Laser Welding of Complex Phase and Dual Phase Advanced High Strength Steels -
The Effects that Welding has on Microstructure and Formability

by

Christopher Kenneth Haines Martin-Root

A thesis
presented to the University of Waterloo
in fulfillment of the
thesis requirement for the degree of
Master of Applied Science
in
Mechanical and Mechatronics Engineering

Waterloo, Ontario, Canada 2020

©Christopher Kenneth Haines Martin-Root 2020

Author's Declaration

I hereby declare that I am the sole author of this thesis. This is a true copy of the thesis, including any required final revisions, as accepted by my examiners.

I understand that my thesis may be made electronically available to the public.

Abstract

To assist in the successful applications of tailor-welded assemblies made from advanced high strength steel (AHSS), there needs to be a thorough understanding of how laser welding process parameters influences the weld cross-section profile, mechanical properties, global formability and local formability performance of the base metal. This study investigates microstructure-formability correlation of fiber laser welds of an un-coated complex phase (CP) AHSS and a hot dipped galvannealed (HDGA) dual phase (DP) AHSS. Both steels were developed to have a minimum tensile strength of 980 MPa, a minimum yield strength of 590 MPa and a minimum total elongation of 12% in the material's transverse direction - 90° to the material's rolling direction.

Tensile tests, limiting dome height (LDH) tests, bi-axial stretch tests, forming-strain analyses, and hole expansion tests (HET) were used to compare base metal (BM) samples to laser welded samples.

The LDH and bi-axial stretch tests showed that, for both materials, the global formability of the welded samples was lower than that of the base metal.

For the CP 980 steel, observations during global formability were correlated to the martensitic-dominant regions within the weld's heat affected zone (HAZ). The welds resisted strain during forming, forcing the surrounding material to accommodate for the restriction. The failure propagated through the path which had the highest about of strain. For the CP steel, this path was through the BM, perpendicular to the welds. Hole expansion tests (HET) showed that the welds significantly decreased the local formability of the BM. Failure during HET initiated in, and

propagated along, the weld HAZ. This was correlated to the microstructures created in the HAZ which were more sensitive to edge stretch failure as compared to the microstructure of the BM.

For the DP 980 steel, observations during global formability tests were correlated to the larger soft region within the weld's HAZ. During forming, strain localized in this zone and caused the material to fail. The failure propagated along the length of the weld which was the path containing the highest about of strain. HET showed that the welds only slightly decreased the local formability of the BM. The failure during HET initiated, and propagated, in the BM rather than the weld. This was correlated to the microstructures created in the HAZ which were less sensitive to edge stretch failure as compared to the microstructure of the BM.

Acknowledgements

I want to express appreciation to my academic supervisors, Professor Dr. Norman Zhou and Professor Dr. Tam Nguyen for their support, mentorship, and flexibility during this research. Their guidance ensured that the process stayed focused, milestones were met, and that the data was presented in a clear, meaningful way.

I would like to thank Stelco Inc. and the Ontario Centres of Excellence for providing financial support for this work.

I would also like to thank Hadi Razmpoosh (CAMJ Ph.D. candidate) who offered countless hours of support through training and the analysis and interpretation of the research data.

Table of Contents

Chapter 1

1.1 Introduction

Automotive manufacturers are constantly considering ways to reduce a vehicle's weight to increase fuel economy while maintaining, or improving, occupant safety. These goals are the result of government regulations developed and enforced by the U.S. Department of Transportation (DOT) and National Highway Traffic Safety Administration (NHTSA). Currently, within the automotive sector, meeting the NHTSA 2025 Corporate Average Fuel Economy (CAFE) standard is a focus and vehicle light-weighting is a method of reaching this goal. The CAFE standard outlines that the fuel consumption of an automotive manufacturer's fleet (between passenger cars and light trucks) shall be 4.32 L/100km (54.5 MPG) by 2025 [1]. Further to this, vehicles must also be designed and constructed with materials that will meet the NHTSA's Frontal, Side Barrier, Side Pole impact requirements [2].

To assist in achieving these stringent targets, automotive companies are looking at reducing the weight of their vehicles by manufacturing components from thinner, but stronger steels. This new group of steels has been classified as Advance High Strength Steel (AHSS). Strategically applying these steels within the structure of a vehicle can reduce the weight by up to 25% [1].

The AHSS portfolio includes Dual Phase (DP) Steel, Complex Phase (CP) Steel, Transformation-Induced plasticity (TRIP) Steel, Ferritic-Bainitic (FB) Steel, Twinning-Induced Plasticity (TWIP) Steel, Martensitic Steel (MS) and Press Hardenable Steel (PHS) [3]. The properties of these different steels are directly related to their unique microstructures. In addition to the separate categories of microstructures available, different mechanical properties exist within the microstructure type. Regardless of the specific type of microstructure, AHSSs are complex materials that are developed using a range of chemical compositions and thermal cycles to obtain the required microstructure which, in turn, creates the required mechanical properties and formability characteristics required for the intended end use.

When AHSS grades are developed by steel companies, the product must satisfy the different chemistry and mechanical property-range constraints outlined by the unique material specifications published by the automotive companies. Some AHSS grades, specifically intended to be used in "cold forming" applications, are characterized by the material's microstructure and minimum tensile strength. The three main microstructures seen in these grades are ferrite, martensite and bainite. A "dual phase" steel has a microstructure consisting predominantly of martensite and ferrite where a "complex phase" or "multi-phase" microstructure will be a combination of martensite, ferrite and bainite. The different microstructures, and their volume fraction, correlate with the mechanical properties of the material. There is a linear relationship between the volume fraction of martensite and the tensile strength of the steel – as the percentage increases so does the strength [4].

Thin gauge, cold forming AHSS is commercially available as a hot dipped zinc coated product and uncoated, cold rolled product. The steel's finished microstructure is developed during their unique final process. Until the final process, the production of the steel, and their process paths are the same:

1. The steel is refined, alloyed and cast;
2. The casting is hot rolled and coiled;

3. The hot rolled coils are processed through an acid solution to remove the oxide layer on the top and bottom surfaces of the coiled material (pickling);
4. The oxide-free coils are then cold rolled and recoiled.

The hot rolling process is not capable of reducing the gauge of the material enough to benefit weight reduction applications. The cold rolling mill is used to reduce the coil to a thin, usable gauge. After cold rolling, the process path changes depending on the coating requirements of the finished product. If the product needs to be hot dipped zinc coated, the cold rolled steel is processed on a continuous galvanizing line (CGL). If the product needs to be bare (uncoated) the cold rolled steel is processed on a continuous annealing line (CAL). The CGL and the CAL processes have inherent differences in their heating and cooling capabilities, which are critical in developing the required final microstructure and associated mechanical properties of the steel. These thermal cycle differences can be compensated for by varying the alloying strategies of the steel. Consequently, steels with the same mechanical properties, but different corrosion protection, could have a different chemistry and a different final microstructure.

Since steel producer's equipment and processing capabilities differ from one another, each facility will align their alloying strategies to suit their individual needs. Therefore, when comparing products of the same AHSS grade from one steel supplier to another, the material will meet the criteria outlined within an industry or customer specification but could have different chemistries, microstructures and mechanical properties. Subsequently, if material is sourced from multiple steel suppliers for a certain component, these potential variations can pose a problem for manufacturers during welding and/or stamping. Differences in material should be understood and taken into consideration when designing the component, the tooling for manufacturing and the weld procedures for assemblies.

Understanding that there can be microstructure and chemistry differences between commercially available AHSSs of the same grade, and that these differences will influence the material's response to formability and welding, research was conducted on two different AHSS steels, both of which were produced by the same North American, integrated steel company. The two steels were developed to have a minimum tensile strength of 980 MPa, a minimum yield strength of 590 MPa and a minimum total elongation of 12% in the material's transverse direction - 90° to the rolling direction. The difference is that, even though the mechanical properties were similar, one steel was developed to be an uncoated product and the other was developed to be a hot dipped, zinc coated product.

1.2 Objective

The objective of this thesis was to understand the fundamental differences between the two steels of interest and how this information can be translated into practical, industry-relevant solutions. The work in this study was novel since an analysis at this level has not yet been performed on these unique steel developments. The knowledge gained through this research can assist in the proper application of these types of steels, which can mitigate costs for end-user. This was accomplished by the following:

1. Characterize the two base metals with respect to their chemistry, microstructure, mechanical properties and formability;
2. Determine an optimum fiber-laser welding process for "Bead-On-Plate" welds for each of the steels and;
3. Document the effects the weld had on the mechanical properties, global formability and local formability of the base metals.

Chapter 2

2.0 Literature Review

2.1 Advanced High Strength Steel Overview

2.1.1 Microstructure and Mechanical Properties of Advanced High Strength Steels

Advanced High Strength Steel (AHSS) have gained popularity with automotive companies due to their high tensile strengths and improved formability over conventional High Strength Low Alloy (HSLA) steels. HSLA steels are single phase, low carbon steels [5] that are strengthened though alloying, substitutional solution strengthening, interstitial solid solution strengthening and grain size refinement [3]. AHSS gain their strength and formability characteristics through the development of different phases within the steel's microstructures. There are currently 7 common AHSS groups being applied in the automotive industry.

Ferritic Bainitic (FB) Steels have a ferrite and bainite microstructure. FB steels are strengthened through grain refinement and the presence of bainite. These steels are used in applications which require high strength and high levels of edge stretch. [3]

Transformation Induced Plasticity (TRIP) Steels have a retained austenite, ferrite, martensite and bainite microstructure. During strain, the retained austenite transforms to martensite. This characteristic produces a high rate of material work hardening which allows these steels to absorb high levels of energy during deformation [3].

Martensitic (MS) Steels have a full martensite microstructure with potentially small traces of ferrite and/or bainite. The martensite-dominated microstructure gives these steels their high strength. Martensitic steels are used in applications which require extremely high levels of strength [3].

Twinning Induced Plasticity (TWIP) Steels have a full austenite microstructure at room temperature. The microstructure of TWIP steels is refined as it strains. This produces a high instantaneous hardening rate. TWIP steels have excellent stretch performance coupled with high strength [3].

Hot Formed (HF) or Press Hardened (PH) Steels obtain their final microstructure, and associated mechanical properties, through a heat treatment cycle during the forming of a finished component. The microstructure and associated strength levels of these components would be comparable to martensitic steels [3].

Dual Phase (DP) Steels have a ferrite and martensite microstructure. DP steels are strengthened by the presence of dispersed martensite through the microstructure. DP steels have very good work hardening rates and elongation performance as compared to HSLA steels with similar yield strengths. They also have an improved yield/tensile strength ratio over HSLA steels [3].

Complex Phase (CP) Steels have a ferrite, martensite and bainite microstructure with potential traces of retained austenite and pearlite. CP steels are strengthened through the presence of martensite and bainite. CP steels have an improved yield/tensile strength ratio over DP steels and they also have improved edge stretch performance over DP steels. These steels are able to absorb high levels of energy during deformation [3].

Figure 2.1 shows where the different AHSS groups would be in relation to each other with respect to the material’s tensile strength vs. its elongation.

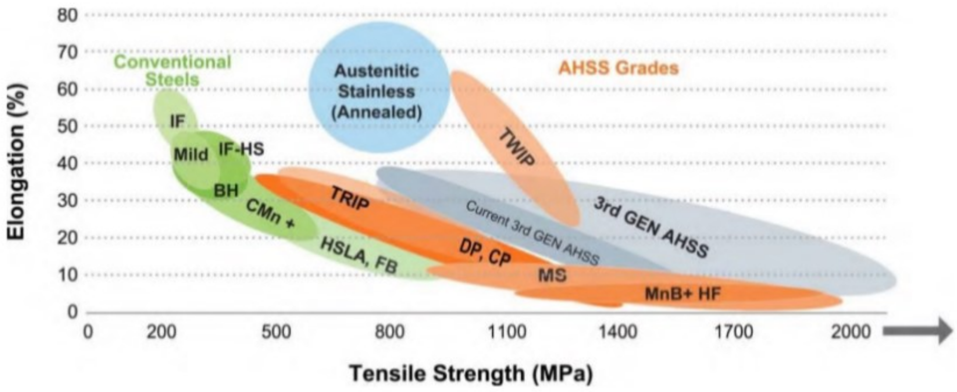

Figure 2.1: Relationship between Tensile Strength vs. Elongation performance of AHSS groups [3].

Dual phase (DP) steels are popular with automotive companies due to their advantages over traditional HSLA steels. The microstructure of DP steel consists of a ferrite matrix with martensite islands dispersed through the matrix. The soft ferrite improves formability and the martensite particles add strength [3].

There are different strengths of DP steels commercially available and are traditionally characterized by their minimum tensile strength – measured in Megapascals (MPa). The 3 main DP steels are 590 DP, 780 DP and 980 DP.

For each of the different strength levels, the volume fraction of martensite particles can range from 20% to 70% [6]. There is a linear relationship between the volume fraction of martensite within a steel's microstructure and the tensile strength of the steel – the higher the martensite content, the higher the tensile strength [4], [7].

Complex Phase (CP) steels are gaining marketshare due to their formability characteristics as compared to DP steels [3]. CP steels can have the same mechanical properties as a DP steel but its microstructure can contains ferrite, martensite, bainite and retained austenite. They are categorized by their minimum tensile strength, the same way DP steels are categorized.

The 3 main CP steels commercially available are 780 CP, 980 CP and1180 CP.

Even though DP and CP steels are classified by their minimum tensile strength, they are also required to meet minimum yield strength and total elongation performance all while adhering to the alloying constraints outlined within different customer and industry specifications. The minimum yield strengths of the steels within the AHSS groups - and the associated minimum tensile strength – can vary. This depends on the application of the steel or on the customer's specification.

To produce DP and CP microstructures, the steel is subjected to a controlled heating and cooling cycle. The heating portion of the cycle involves increasing its temperature to the inter-critical region within the Iron-Iron Carbide (Fe - Fe_3C) phase diagram - between the A_{C1} temperature and the A_{C3} temperature - where the phases are ferrite and austenite (α and γ) [4] – outlined in Figure 2.2.

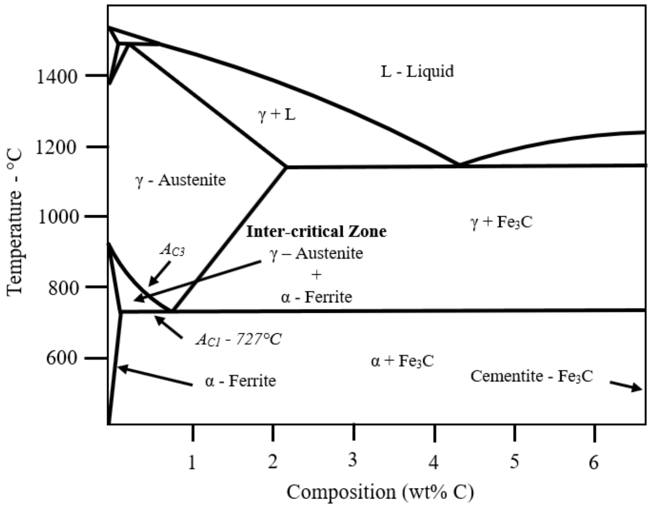

Figure 2.2: Adapted Fe - Fe_3C Phase diagram highlighting the A_{C1} and A_{C3} lines along with the Inter-critical zone.

The steel is then cooled in a precise manner to develop the required final microstructure containing specific volume fractions of ferrite and martensite for DP steels and ferrite, martensite and bainite for CP steels.

2.1.1.1 Ferrite

Ferrite is a stable microconstituent at room temperature. The crystal structure of ferrite is Body Centered Cubic (BCC) meaning that the structure has atoms at all four corners and one atom in the middle. This arrangement makes all the sides of the crystal equal in length. Figure 2.3 (a) is a graphical representation of the BCC crystal structure. The maximum solubility of carbon in a BCC structure is low as the close-packed structure makes it difficult to contain a Carbon atom [5], [8]. Because of this incompatibility, it can be inferred that ferrite will have the comparable mechanical properties to pure iron [9]; a tensile strength of 262 MPa, yield strength of 130 MPa and total elongation of 45% (50mm gauge length) [5].

2.1.1.2 Martensite

Martensite is a non-equilibrium, single phase micro constituent that is the result of a diffusion-less transformation from austenite during rapid cooling /quenching. Martensite is brittle, has low fracture toughness and is the hardest structure that austenite can transform into during cooling [6], [9].

The crystal structure of martensite is Body Centered Tetragonal (BCT) which is similar to the BCC structure but has elongated sides due to carbon atoms captured within the lattice. Figure 2.3 (b) is a graphical representation of the BCT crystal structure. The strength of martensite is directly proportional to its carbon content [4].

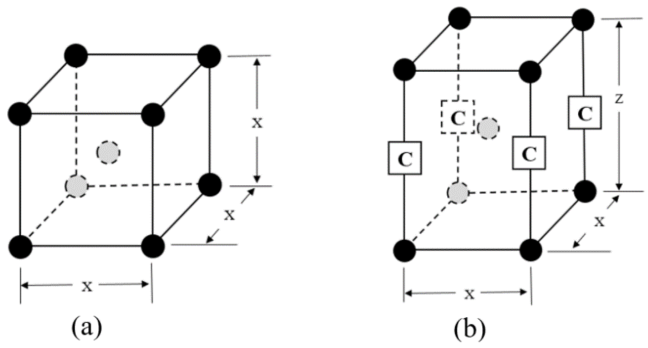

Figure 2.3: BCC (a) and BCT (b) structures. Compared to the BCC crystal structure, the BCT has elongated sides due to the presence of Carbon atoms.

2.1.1.3 Tempered Martensite

The BCT structure of martensite causes it to be unstable and susceptible to tempering – which is the diffusion of the carbon atoms into the surrounding matrix, creating carbides [10] . Properties of the tempered martensite are related to the tempering temperature and the exposure time. There are 4 stages of martensite tempering which are outlined in Table 2.1.

Table 2.1: Overview of the four stages of tempering of Martensite [4]

Stage I (0°C < T < 250° C) • Precipitation of carbides and partial loss of martensite tetragonality. Excess carbon in martensite may partition slowly into residual austenite;
Stage II (200°C < T < 300° C) • Decomposition of retained austenite;
Stage III (250°C < T < 350° C) • Replacement of carbides by cementite &; • Complete elimination of martensite tetragonality;
Stage IV (350°C < T < 700° C) • Coarsening and spheroidizing of cementite &; • Recrystallization of ferrite, which replaces martensite.

Since the strength of martensite is directly proportional to its carbon content within the crystal structure [4], diffusion causes the strength of the tempered martensite to be less than the original martensite.

2.1.1.3 Bainite

Bainite is a eutectoid phase that forms at a lower temperature than pearlite and at a higher temperature than martensite [11]. The microstructure of bainite consists of ferrite and cementite [8]. Depending on the thermal cycle, bainite forms as needles or as plates. At lower temperatures, the bainite is made up of fine carbides dispersed among ferrite plates and is referred to as lower, fine or acicular bainite [8], [11]. At higher temperatures, the bainite is made of ferrite needles with iron carbides [11] and is referred to as upper or feathery bainite [8]. Bainite is able to absorb more energy than tempered martensite [12].

2.1.1.4 Tempered Bainite

Reheating, or tempering, has a different effect on bainite as compared to martensite. The solid solution Carbon present in martensite – which gives it its strength - is not present in bainite because during the formation of bainite, the Carbon precipitates out as carbides [12]. The minor change in strength caused by the tempering of bainite is produced though Fe_3C coarsening and dislocation recovery [12]. The strength of bainite significantly decreases only when the microstructure coarsens or when the bainite plates are replaced by equiaxed grains of ferrite, which is seen during recrystallization [12].

2.1.2 Hot Dipped, Zinc coated AHSS compared to Cold Rolled, Uncoated AHSS

Cold forming AHSS is commercially available as a hot dipped zinc coated (galvanized: HDGI or galvannealed: HDGA) product or a cold rolled (CR) uncoated product. Traditionally, these two products are produced on unique processing lines. The coated product is processed on a continuous galvanizing line (CGL) and the bare product is produced on a continuous annealing line (CAL). The difference between HDGA and HDGI is, for the HDGA product, the steel strip is reheated after the zinc has been applied. This reheating anneals the zinc coating and causes iron from the steel sheet to diffuse into the zinc coating creating an iron-zinc coating [13]. The specific end-use application is a factor for determining if the steel needs to be coated (HDGA or HDGI) or bare. In applications where the steel will not be exposed to moisture, or where the extra cost of a zinc coating won't be incurred, bare material can be used.

In both cases, the steel's finished microstructure is created by heating the steel into its inter-critical region of the Fe - Fe_3C diagram- between the A_{C1} temperature and the A_{C3} temperature. At this temperature, the phases are ferrite and austenite [4]. Once the steel is within the inter-critical temperature zone, it is rapidly cooled in a controlled manner so the ferrite (α) remains but the austenite (γ) transforms into martensite for DP steels [6] [4] or martensite and bainite for CP steels – See Figure 2.2. There are many factors that affect the austenite phase within the inter-critical zone which directly influences the finished microstructure.

As outlined in previous sections, there are a number of variables that need to be considered during product development including, but not limited to, the processing line heating rate, the target temperature range within the inter-critical zone, the size and shape of the material's inter-critical zone, how long the steel is kept in the inter-critical zone, the non-isothermal cooling profile, the alloy chemistry, the cold-rolled full-hard microstructure and the carbon content of the steel [4].

These factors are all interdependent and, since the coating and annealing processing lines throughout the world have different heating and cooling capabilities, there is no guarantee that the alloying strategies of the same grade of AHSS will always be the same. This means that not all products are, or can be, processed the same way. Alloying strategies and heat treatment cycles developed for unique galvanizing or annealing lines may only make the desired microstructures and associated mechanical properties associated with that process path and are not necessarily transferrable from one facility to another. The consequence of this is, depending on which facility produced the steel, the same grade steel can meet a specification but could have different alloying ranges, mechanical properties and volume fractions of different microconstituents.

2.1.3 Effects of Alloying Elements on Processing Parameters and microstructure of AHSS

To achieve the desired microstructure, DP steels are highly alloyed, as alloy elements make up more than 1% of their total weight [6]. The alloying strategies are determined by the steel producer but are constrained by percentage ranges outlined by the industry or customer material specifications - and not all chemistry limits are the same from specification to specification. This means that one alloying strategy might not meet all the requirements for the other specifications. This can make it difficult for product development metallurgists to develop a one-size-fits-all product.

Carbon content plays a significant role in the transformation of austenite to martensite. When referencing the Fe - Fe_3C phase diagram- Figure 2.2, as the temperature is increased from the A_{C1} line to the A_{C3} line, the percentage of austenite also increases until the the A_{C3} line is surpassed, where austenite is the only phase present. The Carbon content within the austenite decreases as the temperature deviates from the A_{C1} temperature and approaches the A_{C3} temperature. Within the inter-critical zone, the austenite has a maximum amount of Carbon at low inter-critical temperatures and a minimum amount of Carbon at high inter-critical temperatures. This relationship highlights the importance of the re-heat temperature range and how it creates available austenite that can be transformed to martensite and/or bainite. It also shows the relationship that the Carbon content of the austenite has on the hardenability of the austenite that is present.

Alloying elements either raise or lower the A_{C1} temperature of steel, depending on the element. Alloying elements that lower the A_{C1}temperature are referred to as *austenite stabilizers.* These elements increase the area of the inter-critical zone where austenite is stable. Alloying elements that raise the eutectoid temperature are referred to as *ferrite stabilizers.* These elements have the opposite effect of austenite stabilizers by decreasing the inter-critical zone where austenite is stable [14].

Mathematical models have been derived from empirical data to predict the A_{C1} and A_{C3} temperatures based off the percentage weight of the alloying elements in the steel. The Andrews model, outlined in Eq. 2.1 and Eq. 2.2 [15], [16], is one example of calculating Ac_1 and Ac_3 using wt.% values of each element.

$$Ac_1 = 723 - 10.2Mn - 16.9Ni + 29.1Si + 16.9Cr + 290As + 6.38W \qquad \text{(Eq. 2.1)}$$

$$Ac_3 = 910 - 203\sqrt{C} + 44.7Si - 15.2Ni + 31.5Mo + 104V + 13.1W - 30Mn + 11Cr + 20Cu - 700P - 400Al - 120As - 400Ti \qquad \text{(Eq. 2.2)}$$

This model predicts the effects that specific alloying percentages have on the Ac_1 and Ac_3 lines which, directly affect the size and shape of the inter-critical zone. In this model, Manganese and Nickel lower the Ac_1 temperature (austenite stabilizers) and Silicon and Chrome increase it (ferrite stabilizers). Carbon, Nickel, Manganese, Aluminum and Titanium decrease the Ac_3 temperature and Silicon, Molybdenum, Vanadium and Chrome increase it. Alternate Ac_1 and Ac_3 temperature models have been developed since the Andrews model [16].

Adding alloying elements can have other purposes other than moving the A_{C1} line. They also effect the eutectoid Carbon content [17]. Alloy elements not only effect the hardenability of the austenite during the cooling portion of a heat treatment but, since they are attracted to Carbon, they also create complex carbides within the composition [17].

Alloy elements change the steel’s Time-Temperature-Transformation (TTT) and Continious-Cooling-Transformation (CCT) diagrams. Depending on the alloy added, the diagram’s profile shape is changed, shifted or both. These changes affect the hardenabiltiy of a steel and also change the start and finish temperatures of the different microstructures i.e. pearlite, bainite and martensite [5], [14]. It has been shown that Carbon, Manganese, Chromium and Silicon have the greatest effect on the martensite start temperature (M_S) and that Carbon and Manganese have the greatest effect on the bainite start temperature (B_S) [4], [15], [18].

The heating and cooling cycles of AHSS can be complex, involving multiple stages of heating, temperature holding and cooling. For DP steels, the important phase transformation occurs when the steel is rapidly cooled from the inter-critical temperature zone to a temperature which starts transforming austenite to martensite. This cooling needs to be fast enough to prevent the formation of unwanted phases (pearlite and bainite). For CP steels, the cooling vs. time profile needs cross the bainite start (B_S) line then the M_S line to produce the 3 phases.

The heating and cooling capabilities of available CGL and CAL are used to develop the chemistry ranges for the specific grade of AHSS. There are conflicting contsraints when developing the alloy strategy. The alloy percentages need to adhere to the limits outlined by the customer, they must be able to produce the desired microstructure & strength and their cost needs to be commercially viable.

2.1.4 Formability of DP and CP AHSS

The mechanical properties associated with AHSS, along with their unique microstructures, causes these steels to have different forming characteristics as compared to HSLA steels. As tensile and yield strengths elevate, forming becomes more difficult. There are two areas of formability which are used to describe the limits of sheet steel deformation at failure. These areas are *Global Formability* and *Local Formability*.

Global formability refers to the stretch-deformation limit that the body of the sheet metal can undergo before failure. Global formability of a material can be evaluated by using a Limiting Dome Height test (LDH) and by Stretch Forming Limit tests [19].

Global formability is directly correlated to a material strain hardening characteristic. Strain hardening is the phenomenon which describes the increase of a material's strength as it is plastically deformed [8]. This hardening characteristic is typically obtained from curve fitting a true stress vs. true strain curve. The n-value can also be defined as the effective, true strain at the material's ultimate tensile strength [20]. A material's n-value describes how it distributes strain when stress is applied. As a material's n-value increases, it indicates that the material is better at distributing strain. This is achieved by the material thinning over a region as compared to the thinning focusing on a small area. When the strain and cross-section thinning become localized, the material necks. The necked area becomes a weak point where all the strain concentrates, resulting in splitting of the material in that area [6], [21].

Local formability refers to a material's edge stretching limit [3]. For the failure to be considered an edge stretch issue, it must initiate at an edge and not within the body of the material. Local formability is evaluated by using the Hole Expansion Test (HET). This test flanges a 10mm hole that is pierced in a metal sample. The flanging process stretches the material as it increases the hole's diameter/circumference. The test is complete when a through-thickness crack appears in the material. The diameter of the hole at failure is compared to the original diameter and the hole expansion ratio (HER) is calculated [22]. This ratio is used to compare the edge stretch formability of different materials.

The ferrite-martensite microstructure of DP steels offers a formability advantage over HSLA steels. When DP steels are exposed to stress, the strain disperses through the ferrite phase which has good ductility since it is soft and malleable [3]. The combination of the ferrite and martensite matrix produces a higher n-value as compared to HSLA steels with similar tensile and yield strengths [3], [6], [21].

The ferrite, martensite and bainite microstructure of CP steels was not developed to improve the strain hardening performance of a high strength steel. CP steels tend to have lower elongation values and a higher yield-to-tensile strength ratio when compared to DP steels [4] [6]. The benefit of a CP steel's microstructure lies in edge stretch performance, which is superior to dual phase steels [4]. Studies have showed that when the hardness difference between the phases within the steel's microstructure's increases, the edge stretch performance decreases [23]. This is important when predicting how an AHSS will respond to edge stretch during deformation seen in stamping, roll forming or bending operations. A DP microstructure has a significant difference in the hardness of the soft phase and hard phase. The microstructure of CP steels highlights why these steels exhibit superior edge stretch performance. It has been seen that the presence of bainite, which has a hardness between ferrite and martensite, increases edge stretch performance [24]–[27].

2.2 Laser Welding

The use of lasers for welding has gained popularity in industrial applications due to its high-power capabilities which can be concentrated into a small beam diameter, enabling faster welding speeds.

The process of producing laser light involves pumping energy (light, electric current, or chemical/nuclear reaction) into a special *medium*. The energy raises some of the medium's atoms to an excited state. The excited atoms within the medium release photons and these emitted photons stimulate additional atoms which also emit photons with the same wavelength. This process continues, amplifying the number of photons contained in the medium. The photons are reflected back-and-forth between mirrors located at either end of the medium. One mirror is fully reflective and the other is semi-reflective. When the amplification reaches a critical level, a beam of photons (laser beam) pass through the semi-reflective mirror [8], [28], [29]. The medium used in the system determines the laser beam wavelength. Typical mediums are: Solid-state (neodymium-doped yttrium aluminum garnet (Nd: YAG) and ruby doped with Cr_2O_3), Gas (CO_2 and He and N) and, semiconductor based on GaAs solid solutions (Diode) [28], [29].

The high energy beam of photons emitted from a laser is parallel, monochromatic and coherent. The coherent nature of the laser light makes the wave-like characteristic in-phase, eliminating potential destructive interference [8].

During the laser welding process, the beam is used to melt the metal(s) and upon solidification, a solid bond is created. Within all finished fusion welds there are 3 main areas created: The fusion zone (FZ) - in the middle of the joint; the heat affected zone (HAZ) - adjacent to the fusion zone on either side of the joint and; the base metal (BM) – which is unaffected by the welding process. These 3 areas are exposed to temperatures ranging from the material's melting point (FZ) to the ambient temperature (BM). The temperature gradient within the FZ and HAZ creates different microstructures due to the heating and cooling (heat treatment) cycles it is exposed to during welding process.

Laser welding is classified as a high energy-density fusion welding technique with welding occurring between 10^3 to 10^5W/mm² [29]. Power density in welding is the amount of power transferred to the workpiece per unit surface area. The time required to melt the workpiece metal is inversely proportional to this power transferred [30]. With such high-power density capabilities, laser welds are narrow, require short interaction times, and allow for high welding speeds. These speeds can reach several meters per minute which makes the total heat input much lower that other types of fusion welding [29]. When the welding speed is reduced, the heat input into the workpiece increases which creates a larger HAZ [31].

2.2.1 Effects of Laser Welding on AHSS

Fusion welding can be used to create butt joints in tailor-welded blank configurations along with finished assemblies made up of AHSS. Tailor welded blanks are used in the automotive industry to create components that have different thicknesses and strengths within the finished part. In addition to this, some parts are welded together after forming to mitigate forming limitations due to part geometry. As previously described, the heat treatment cycles used to create AHSS is complex and sensitive. Since the laser welding process imparts a local thermal cycle on the base metal, the resulting microstructure around the weld join will be greatly affected.

During laser welding, the heat input and cooling rates will dictate the finished microstructure within the weld joint. This thermal cycle time is referred to as the residence time [32]. The residence time is roughly proportional to the heat input rate, which is defined as the heat input divided by the welding speed [33]. During laser welding, the final grain size of the steel will increase as the peak temperature and residence times increase. During a non-isothermal heat treatment of steel, the austenite grain size has an effect on the M_S temperature and that the austenite grain size also changes the morphology of the martensite phase. [34]–[36]

A decrease in residence time will result in a decreased of the overall effect that the heat input has on the steel's microstructure in the FZ and HAZ. This phenomenon was seen in studies comparing welds created using a diode laser and a Nd: YAG laser. The Nd: YAG laser had a higher power input capability than the diode laser and therefore was able to weld at faster transverse speeds which resulted in a shorter residence time [37]. The Nd: YAG laser produced a narrower HAZ as compared to the diode laser [38]. When welding with a laser, the time to melt the workpiece is low and limited heat conduction takes place which increases the cooling rate of the weld. These factors decrease the residence time which makes laser welding an excellent choice for welding heavily alloyed AHSS as it will minimize the size of the HAZ.

Numerous studies have shown that when AHSS is laser welded, the microstructure in the FZ transformed from the original base metal microstructure to 100% martensite [10], [37], [39], [40], which causes the area to have high hardness. When DP steels are laser welded, a soft zone is created within the HAZ. The degree of softening increased, and the size of the soft zone widens, as the strength of the base material increases [41]. The area associated with the HAZ soft zone is subjected to temperatures close to, but not exceeding the A_{C1}temperature. This process tempers the martensite by allowing carbon from the unstable martensite to diffuse into the surrounding matrix creating carbides [10]. As the carbon content of martensite decreases, so does its hardness [4], causing the ductility of the material to increase.

To assist in understanding the weld hardness profile, previous studies have further sub-divided the HAZ into 3 separate areas – based on the microstructures present. The zone immediately adjacent to either side of the FZ was characterized as the Upper-Critical Heat Affected Zone (UCHAZ). The zone immediately adjacent to the UCHAZ was characterized as the Inter-Critical Heat Affected Zone (ICHAZ) and the zone located between to the ICHAZ and the BM was characterized as the Sub-Critical Heat Affected Zone (SCHAZ) [10], [41].

Studies were performed to show the effects of laser welding heat input on the formability and mechanical properties of dual phase steels. The soft zone width increased as the welding speed decreased and that the formability decreased as the soft zone size increased [10], [37].

The different weld zones and the corresponding microstructures are an important part of understanding how a tailor welded assembly, made from DP steel, will response to stress and strain

– both in uniaxial (tensile testing) and biaxial (Limiting Dome Height-LDH) loading. The formation of the soft zone in a welded joint had significant, negative effects on the tensile properties and formability performance of DP steel [10], [37], [40], [42]. In both of these types of tests, the soft zone within HAZ caused the sample to fail at lower strain values – when compared to the base metal [37], [43]. Tensile tests with strain analysis showed that yielding started in the soft zone and that plastic strain concentrated in this area also [37]. During LDH global formability testing of welded DP steels, the sample failed in the soft zone and the failure travelled along the soft zone, regardless of the orientation of the weld to material's rolling direction [43].

The current literature on welding and forming of welded AHSS does not capture all the different grade developments from the steel producers. This leaves a gap in understanding how different steel chemistries and microstructures will perform during commercial applications. There is also an absence in the literature surrounding the effects that laser welding has on the local formability performance of AHSS.

Chapter 3

3.0 Experimental Overview, Equipment and Procedures

3.1 Experiment Overview

To fulfill the objectives of the thesis, the research was divided into two phases and each phase consisted of four activities. The process map, outlined in Figure 3.1, was developed to guide the research.

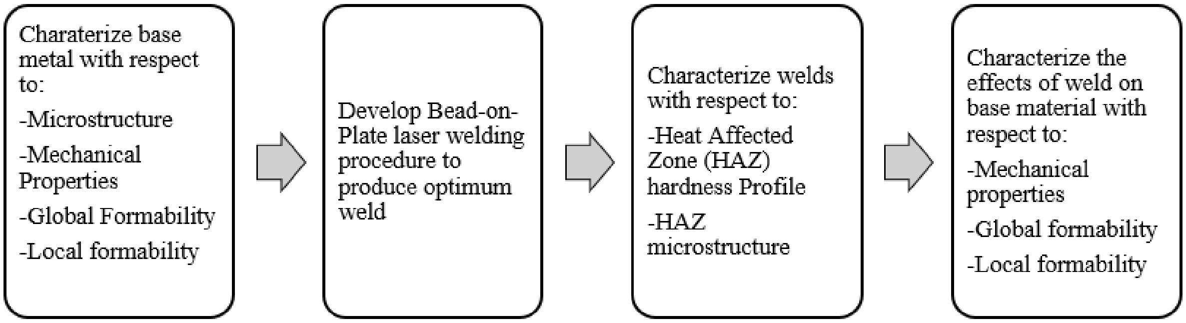

Figure 3.1: Process flow of the 4 activities within the 2 phases of the research project

The first phase of the research focused on characterizing and testing the uncoated, CP 980 steel and the second phase focused on characterizing and testing the HDGA DP 980 steel. Each phase used the same methodology, processing equipment and testing apparatus.

Phases one and two were broken into four discrete activities. The first activity focused on characterizing the base metal's microstructure, mechanical properties, global formability and local formability. This data was later used as a baseline when comparing the effects that the weld had on the base metal.

The second activity concentrated on developing a welding procedure to produce an optimum Bead-on-Plate (BOP) weld for each material. This was done by generating a *Laser Power vs. Transverse Speed* test matrix. These different weld-parameter combinations were used to produce BOP weld on individual steel samples. It has been shown that weld concavity had negative effects on the overall performance of the joints and hence, weld parameters should be developed to minimize it [44], [45]. During this research, the acceptance criteria for an optimum weld procedure must create a weld which exhibited a full through-thickness penetration and minimum weld concavity. The laser's transverse speed was also taken into consideration for determining the best weld procedure. Industrial-relevant speeds needed to be considered, meaning that, if two welds could meet the acceptance criteria for penetration and concavity, the weld produced with the fastest transverse speed was chosen as the optimum weld.

Each sample's weld was sectioned, mounted, polished, etched and analyzed to determine which combination produced a fully penetrated weld with a minimum amount of weld concavity. Once the optimum weld established, it was used in all subsequent activities.

The third activity involved the characterization and documentation of the weld's Heat Affected Zone (HAZ). Micro-hardness testing was used to obtain the hardness profile across the different weld zones. This included the base material, HAZ and FZ on both sides of the weld joint. Using scanning electron microscopy, the microstructures of each zone was identified and correlated to the hardness profile.

In Activity four, welded samples were produced for mechanical property, global formability and local formability testing. For mechanical property testing, samples were welded in the material's longitudinal and transverse direction. The tensile bar profile was positioned so the weld was perpendicular to the direction of the tensile force (See Figure 3.2). For global formability testing, samples were welded in the longitudinal and transverse directions at 0, 13, 19, 25 and 38mm offsets from the center line (See Figure 3.3 (a-e)). These samples were prepared for both the LDH and bi-axial stretch tests. For HET the sample was welded with welds located 45° from each other around the pierced hole, as outlined in Figure 3.3 (f). This created welds parallel to the material's rolling direction, perpendicular to the rolling direction and welds bisecting these 2 directions.

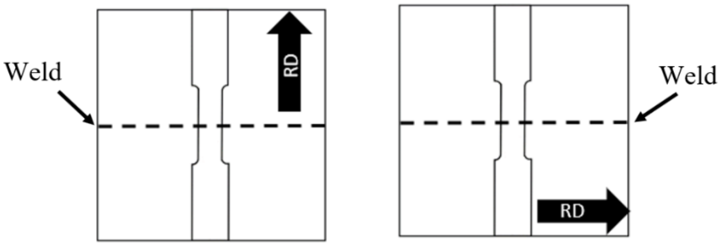

Figure 3.2: Weld orientation with respect to tensile bar profile and the material's longitudinal and transverse direction

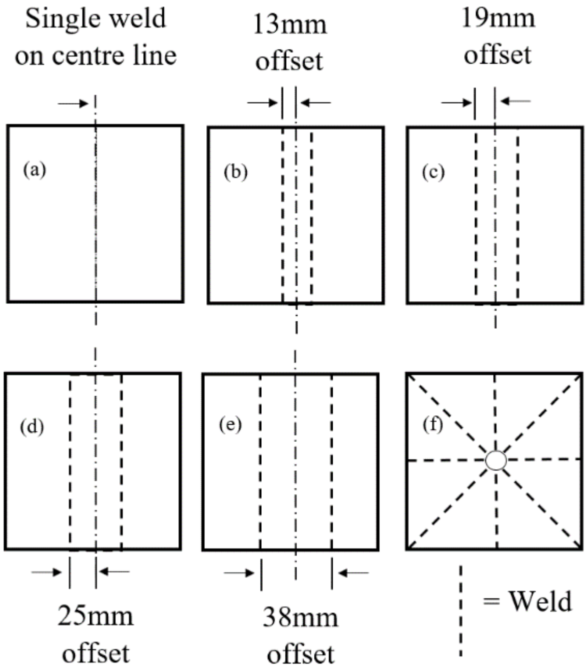

Figure 3.3: Weld layouts used for forming tests. Layouts a - e were used for global formability tests (LDH & bi-axial stretch) and layout f was used for local formability tests (HET)

3.2 Testing Equipment and Test Procedures

3.2.1 Mechanical Property Testing

The yield strength, tensile strength and elongation of the base metal and welded samples were determined through tensile testing. The testing was performed using a universal testing machine and a JIS #5 tensile bar profile [46].

3.2.2 Global Formability Testing

Global formability refers to the stretch-deformation limit that the body of the sheet metal can undergo before failure. Global formability was analyzed using Limiting Dome Height (LDH) tests and bi-axial stretch tests. Both tests involved clamping/binding a flat, 200mm X 200mm (8” X 8”) sample around its perimeter and forcing a 100mm diameter hemispherical punch into the sheet steel to deform it. During the test, the punch speed was held constant at a 0.5mm/second. When the material split, the test was complete. For the LDH test, the forming punch height was zero when it touched the backside of the sample. The final punch height was recorded when the material failed.

The bi-axial stretch test was like the LDH test but used cameras and Digital Image Correlation (DIC) software to calculate the strain in different areas of the sheet steel during forming. This was done by first preparing the samples through painting the surface solid white and then adding a random black speckle pattern to the white base. During testing, the unique black speckles were pixelated, and these pixels were measured in their major and minor axes. The major axis was aligned in the direction that experienced the maximum amount of deformation and the minor axis was 90° to the major axis. The change in dimensions were correlated to the strain in the area of that unique location. With this setup, strain values were measured over different locations of the deformed specimen. During testing, DIC strain measurements were captured using an ARAMIS software and camera system.

The tooling used for the LDH and bi-axial stretch tests was custom made and the tests were performed in a 75T hydraulic press. Figure 3.4 shows the cross-section of the tooling used in these two global formability tests.

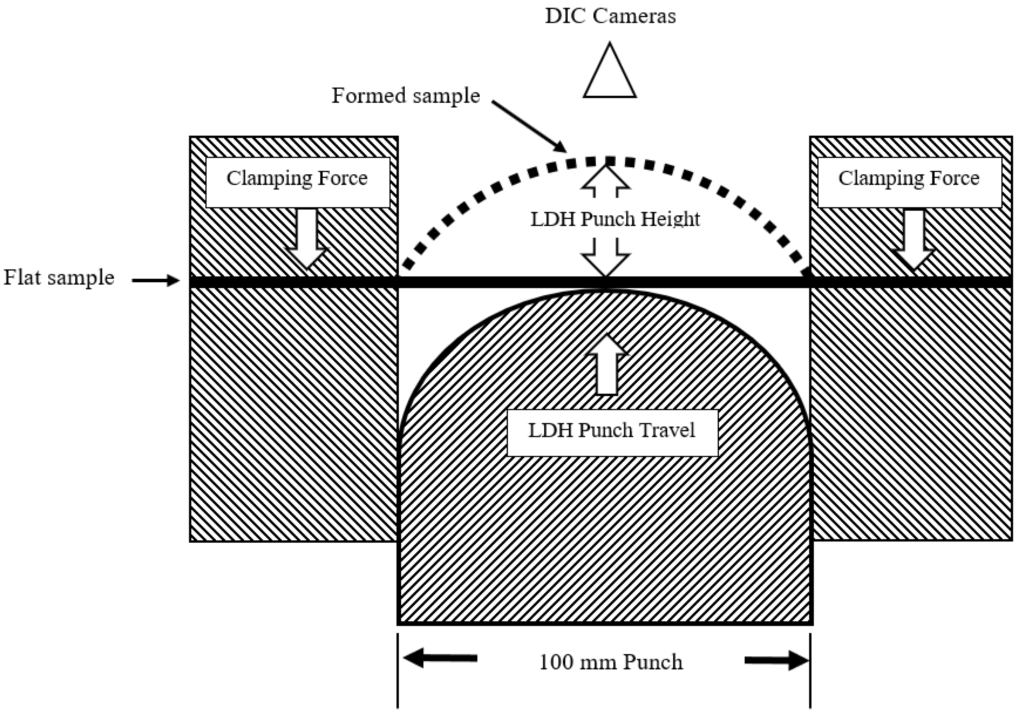

Figure 3.4: Cross Section of LDH and Bi-axial Stretch Test Tooling

3.2.3 Local Formability Testing

Local formability was analyzed using the Hole Expansion Test (HET) outlined in the ISO 16630 standard [22]. This test involved clamping/binding a flat, 200mm X 200mm (8” X 8”) sample around its perimeter and forcing a 60° conical punch through a 10mm pierced hole located in the center of the sample. During the test, the conical punch speed was held constant at a 0.5mm/second. The cone’s movement caused the hole to expand, increasing the diameter and subsequently the hole’s circumference. When the material exhibited a through-thickness crack, the test was complete. Cameras were positioned to monitor the material around the circumference of the hole. At the moment of failure, the still-frame image was used to measure, and calculate and the expansion ratio (λ) by using Eq. 3.1 [22]:

$$\lambda = \left(\frac{D_E - D_0}{D_0}\right) X\ 100\% \qquad \text{(Eq. 3.1)}$$

where D_E is the diameter of expanded hole at failure (mm) and D_0 is the original hole diameter (10mm).

The tooling used for this test was custom made and the test was performed in an *Interlaken 110* press. A cross-section representing the HET tooling and process is shown in Figure 3.5.

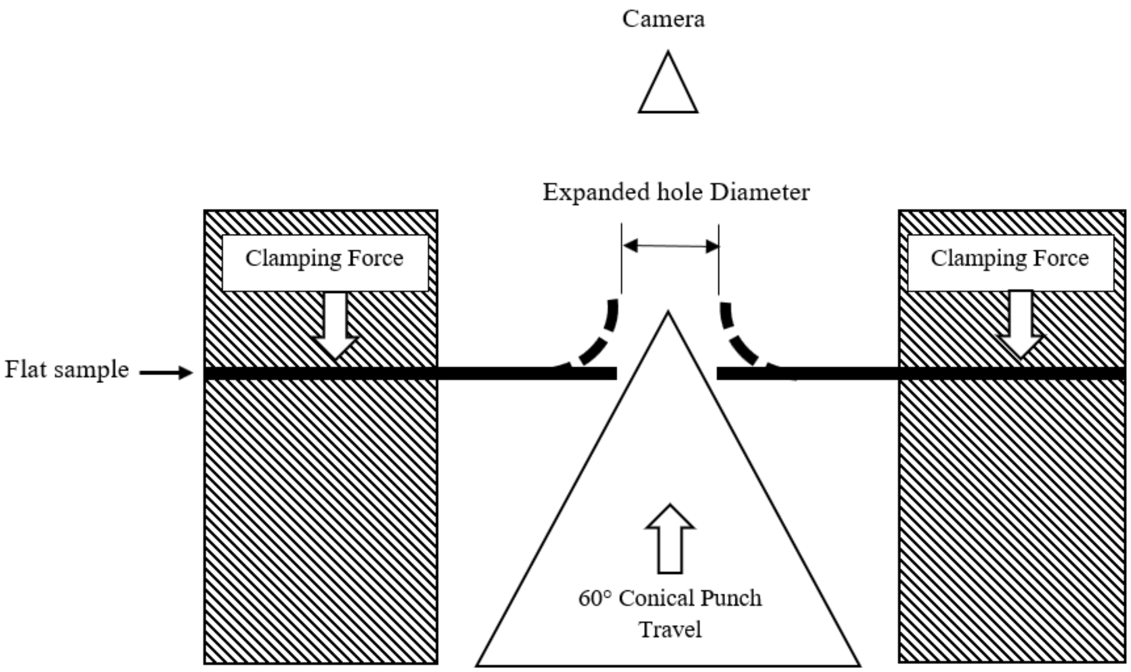

Figure 3.5:Cross-section of Hole Expansion Test Tooling

When the HET was performed on the base material and welded samples, the sample was always oriented so that the shear portion of the pierced hole was against the conical punch. When the hole expansion blanks were welded, the top surface of the weld was on the opposite side of the shear portion of the pierced hole. This orientation is outlined in Figure 3.6.

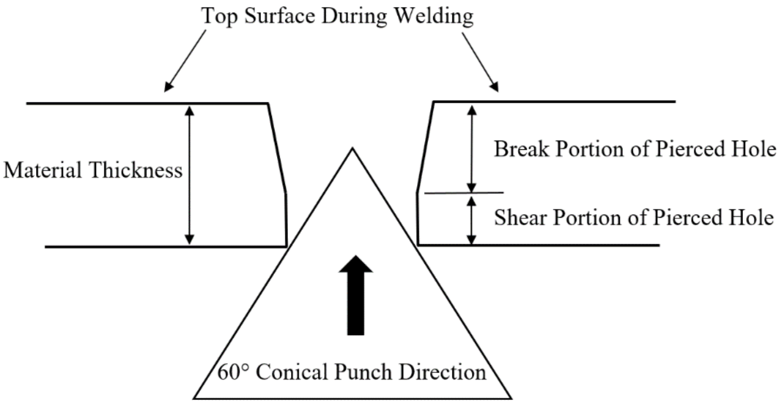

Figure 3.6: Pierced hole shear orientation during HET and the position of the top surface of the weld with respect to the pierced hole cross section.

3.2.4 Laser Welding Equipment

Bead-on-plate (BoP) welds were produced using a Panasonic TA1600 5-axis robot arm and an IPG YLS-6000 fiber laser system with a beam spot-diameter of ~0.6 mm and a wavelength of 1071nm. During welding, 200mm X 200mm (8” X 8”) samples were secured in a fixture that clamped the specimen on either side of the weld path (Figure 3.7). The straight-line weld was exposed to ambient air without the use of additional shielding gas. The laser’s focal point was adjusted so that it was located on the top surface of the steel sample. The clamping strategy ensured that the sample remained flat and that the top surface of the sample remained in-focus from the start of the weld to the finish.

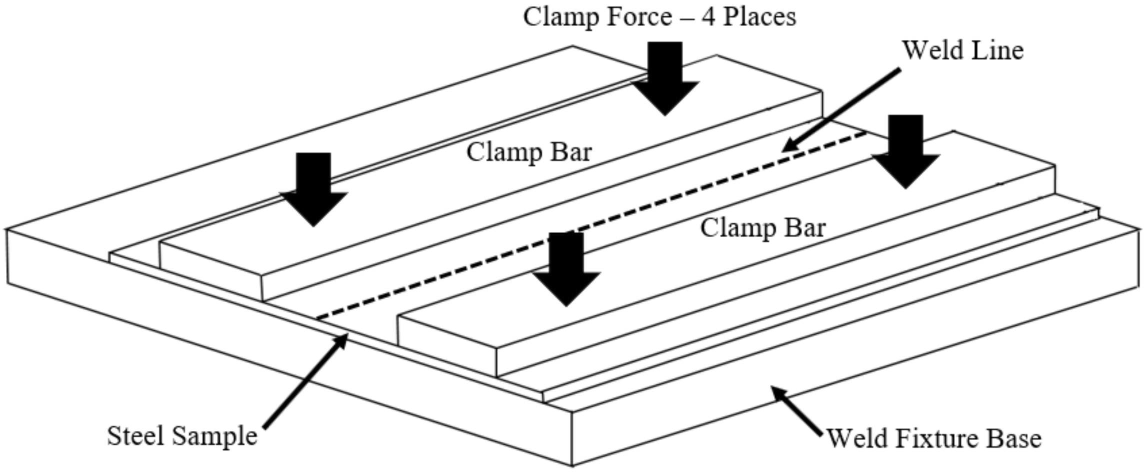

Figure 3.7: Weld Fixture used for laser welding flat steel samples. The sample was clamped on either side of the weld.

3.2.5 Microstructure and Weld hardness profile testing

The base metal microstructure was characterized using a JEOL JSM-6510LV scanning electron microscope (SEM). The volume fraction of the present phases was measured using a grid method outlined in the ASTM E562-11 specification [47].

Each weld was analyzed using conventional sectioning, mounting, polishing, etching (nital 2%) and optical microscopy techniques.

An automated-stage Clemex-JS2000 Vickers micro-indenter was set at a 300gf load and a 10 second dwell time to obtain the microhardness profile across the weld. The testing was done with 2 rows of 25 indentations. The second row was offset to obtain a hardness measurement between the 2 indentations in the previous row. The measurement location layout is shown in Figure 3.8.

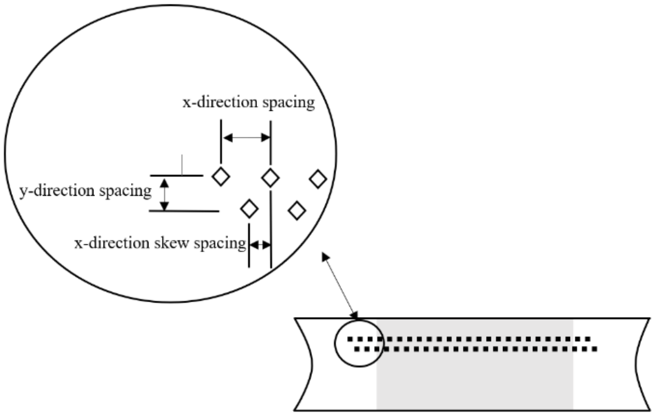

Figure 3.8: Weld microhardness measurement layout

Weld-region microstructures for Phase 1 (CAL product) were characterized by means of a Zeiss-Leo 1530 Field Emission SEM and the weld-region microstructures for Phase 2 (HDGA) were characterized by means of a JEOL-JSM 7000F Field Emission SEM.

Chapter 4

4.0 Observations

4.1 Base Material Characterization

4.1.1 Cold Rolled, Uncoated CP 980 Steel

4.1.1.1 CP 980 Steel Base Metal Microstructure, Chemistry and Mechanical Properties

A commercially available, cold rolled, un-coated 1.6mm thick CP 980 AHSS was used during the first phase of the experiments. This steel was produced in North America at an integrated steel mill. After cold rolling, the final microstructure was created on a horizontal, hydrogen-quench continuous annealing line. The details of the material chemistry and the mechanical properties are outlined in Table 4.1 and 4.2 respectively.

Table 4.1: Chemical Composition (wt.%) of the experimental CP980 AHSS

Element	**C**	**Mn**	**Al**	**Si**	**B**	**Cr + Mo**
wt.%	0.19	1.82	0.046	0.39	0.0003	0.26

Table 4.2: Mechanical Properties (JIS#5) of the experimental CP980 AHSS

	Longitudinal Direction	Transverse Direction
Average UTS (MPa)	1125	1126
Average YS (MPa)	687	726
Average Total Elongation (%)	15	12

The base metal microstructure analysis of this CP steel showed 3 dominant phases: bainite, martensite and ferrite. Bainite had the highest volume fraction percentage with 44%, followed by martensite with 32% and then ferrite with 27%. Figure 4.1 shows a SEM micrograph of the base metal and outlines the 3 main phases and their respective volume fractions. The ferrite phase is dark, the martensite phase is lighter and the bainite phase is dark with light speckles.

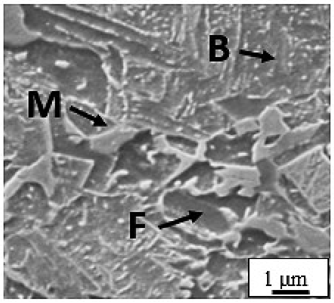

Figure 4.1:SEM Micrograph of Initial Microstructure of CP 980 Material showing 41% Bainite (B), 32% Martensite (M), and 27% Ferrite (F)

4.1.1.2 Global and Local Formability Performance of CP 980 Steel

During LDH testing is was seen that the average height that the 100mm hemispherical punch reached was 35mm. It was observed that the failure (split) initiated on the nose of the punch and propagated parallel to the material’s rolling direction. Figure 4.2 shows the failure of the material from the top view and from the side view of the test sample. During the LDH testing of the CP 980 base metal, the major and minor strain were similar because this is a bi-axial stretch test. Figure 4.3 shows the major-strain distribution across the centre of the punch at the moment just before the material failed.

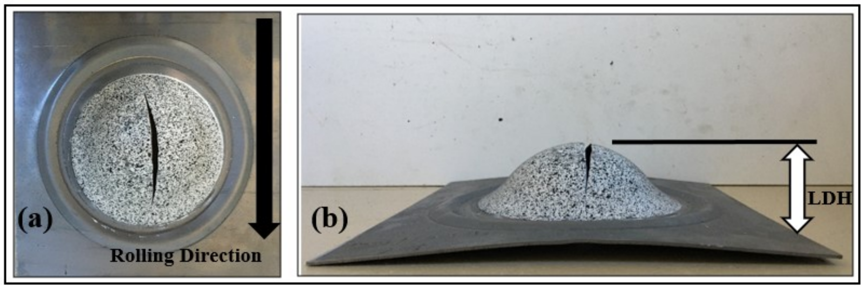

Figure 4.2: LDH Failure on CP 980 base metal. The split initiated at the nose of the punch and propagated parallel to the material's rolling direction. (a)-top surface, (b) - side profile.

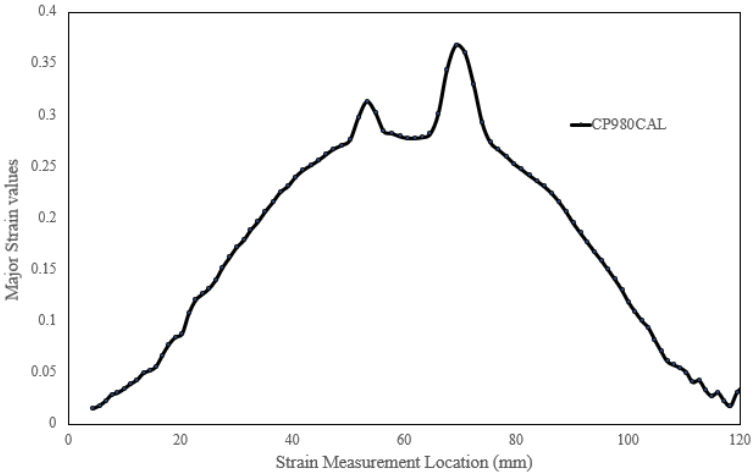

Figure 4.3: Major-strain distribution during bi-axial stretch formability test of CP 980 base material. Strain measurements were taken just before failure.

During hole expansion testing, is was seen that the average edge stretch (λ) was 30%. It was observed that the failure (split) initiated and propagated parallel to the material's rolling direction which was similar to the failure direction seen in the global formability test.

4.1.2 Hot Dipped Galvanealed (HDGA)DP 980

4.1.2.1 DP 980 Base Metal Microstructure, Chemistry and Mechanical Properties

A commercially available, HDGA 1.0 mm thick DP 980 AHSS was used during the second phase of the experiments. This steel was produced in North America at an integrated steel mill. After cold rolling, the final microstructure was created on a continuous galvanizing/galvanealing line. The details of the material chemistry and the mechanical properties are outlined in Table 4.3 and 4.4 respectively.

Table 4.3: Chemical Composition (wt.%) of the experimental DP980 AHSS

Element	**C**	**Mn**	**Al**	**Si**	**B**	**Cr + Mo**
wt.%	0.15	2.58	0.046	0.11	0.0003	0.35

Table 4.4: Mechanical Properties (JIS#5) of the experimental DP980 AHSS

	Longitudinal Direction	Transverse Direction
Average UTS (MPa)	1159	1143
Average YS (MPa)	672	690
Average Total Elongation (%)	11	14

The base metal microstructure analysis of this material showed 2 dominant phases: martensite and ferrite. Martensite had the highest volume fraction percentage with 66% and the ferrite phase was 34%. Figure 4.4 shows a SEM micrograph of the base metal and outlines the 2 phases and their respective volume fractions. The ferrite phase is dark, and the martensite phase is light.

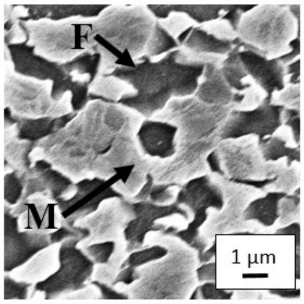

Figure 4.4: SEM micrograph of Initial Microstructure of DP 980 Material Showing 66% Martensite (M) and 34% Ferrite (F)

4.1.2.2 DP 980 Global and Local Formability Performance

During LDH testing is was seen that the average height that the 100mm hemispherical punch reached was 22mm. It was observed that the failure (split) initiated on the nose of the punch and propagated parallel to the material's rolling direction. Figure 4.5 shows the failure of the material from the top view and from the side view of the test sample. The major strain was measured across the dome of the punch during forming. Figure 4.6 shows the major-strain distribution across the centre of the punch at the point just before the material failed.

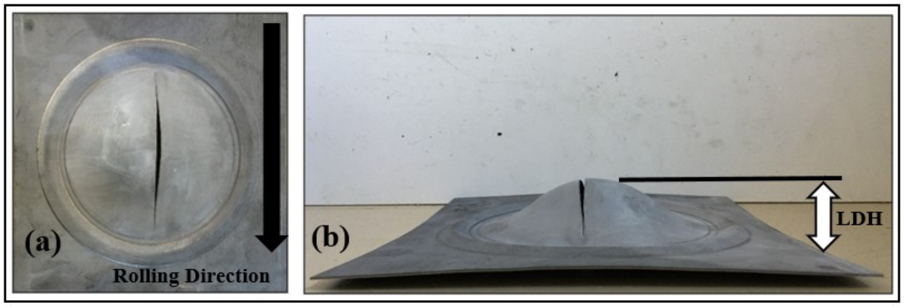

Figure 4.5: LDH Failure on DP 980 BM. The split initiated at the nose of the punch and propagated parallel to the material's rolling direction. (a)-top surface, (b) - side profile.

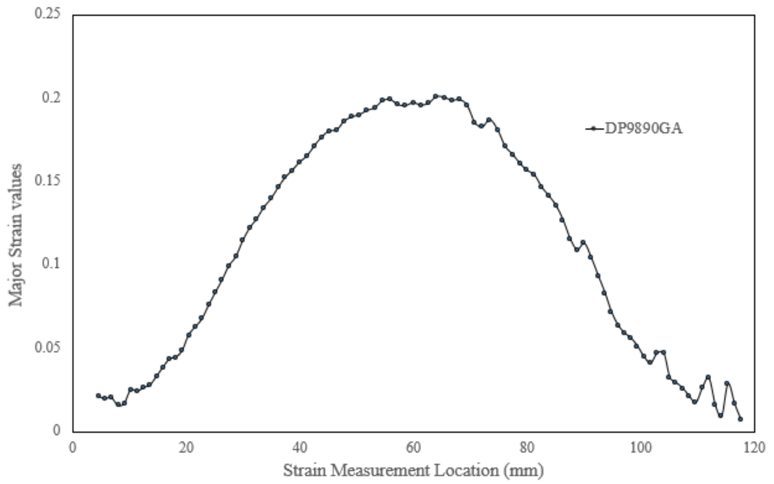

Figure 4.6: Major-strain distribution during bi-axial stretch formability test of DP 980 BM. Strain measurements were taken just before failure.

During hole expansion testing, is was seen that the average edge stretch (λ) was 11%. It was observed that the orientation of the failure (split) was random with respect to the material's rolling direction.

4.2 Weld Procedure Development and Weld Characterization

4.2.1 Cold Rolled, Uncoated CP 980 Steel Weld Procedure Development

Figure 4.7 outlines the cross-sections of the welds produced at different laser powers and transverse speeds with the CP 980 steel. During welding it was observed that, for each laser power level, as the transverse speed increased, the weld reached a point where the penetration became incomplete. This can be seen on the welds produced at 2kW-10m/minute, 3kW-15m/min, 4kW – 18m/min and 6kW – 26m/minute.

It was also observed that as the welding power increased, the tendency of the weld to exhibit concavity also increased due to vaporization of the material. The welds produced at 2kW showed little-to-no concavity. At 3kW, the welds started showing the presence of concavity. The concavity was more prevalent in the higher welding powers that were coupled with slower transverse speeds. This can be seen on the welds produced at 5kW-16m/minute and 6kW-20m/minute.

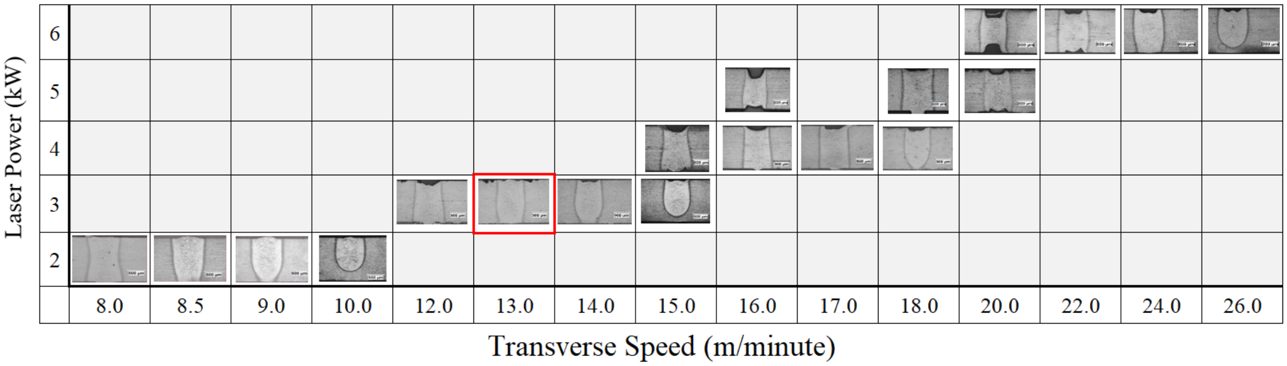

Figure 4.7: Weld cross-section charts showing different Laser Power vs. Transverse Speed combinations in the CP 980 material. The weld produced using 3 kW at 13m/minute was chosen as the optimum weld (exhibiting full BM penetration with minimum concavity). This weld parameter combination was used for the remainder of the research with this material.

Using the criteria outlined above in section 3.1, the weld that was produced with a welding power of 3kW and a transverse speed of 13m/s was chosen as the best weld and was used for the remainder of the research testing.

4.2.1.1 Mechanical Properties of Welded CP 980 Material

To determine if the HAZ of the weld introduced detrimental effects on the overall performance of the joint, welded coupons were prepared for uniaxial tensile testing with welds positioned perpendicular, and parallel to the material's rolling direction – See Figure 3.2. Aside from being able to compare the mechanical properties of the welded samples to the base material, the test was also used to determine where the tensile failure occurred. On the samples welded with 3kW and 13m/minute, the failures occurred in the base metal of the gauge length and not at the weld.

Figures 4.8 shows the individual average engineering stress-strain graphs for the base metal and the welded samples. The longitudinal direction implies that the rolling direction is parallel to the tensile specimen axis and the transverse directions implies that the rolling direction is 90° to the tensile specimen. In all cases, the welds are always perpendicular to the axis of the specimen – see Figure 3.2. For comparison purposes, Figure 4.9 combines Figures 4.8 (a)-(d) onto one plot. In all cases the tensile tests showed a decrease in total elongation on the welded samples. The yield strengths and tensile strengths were similar for all the samples.

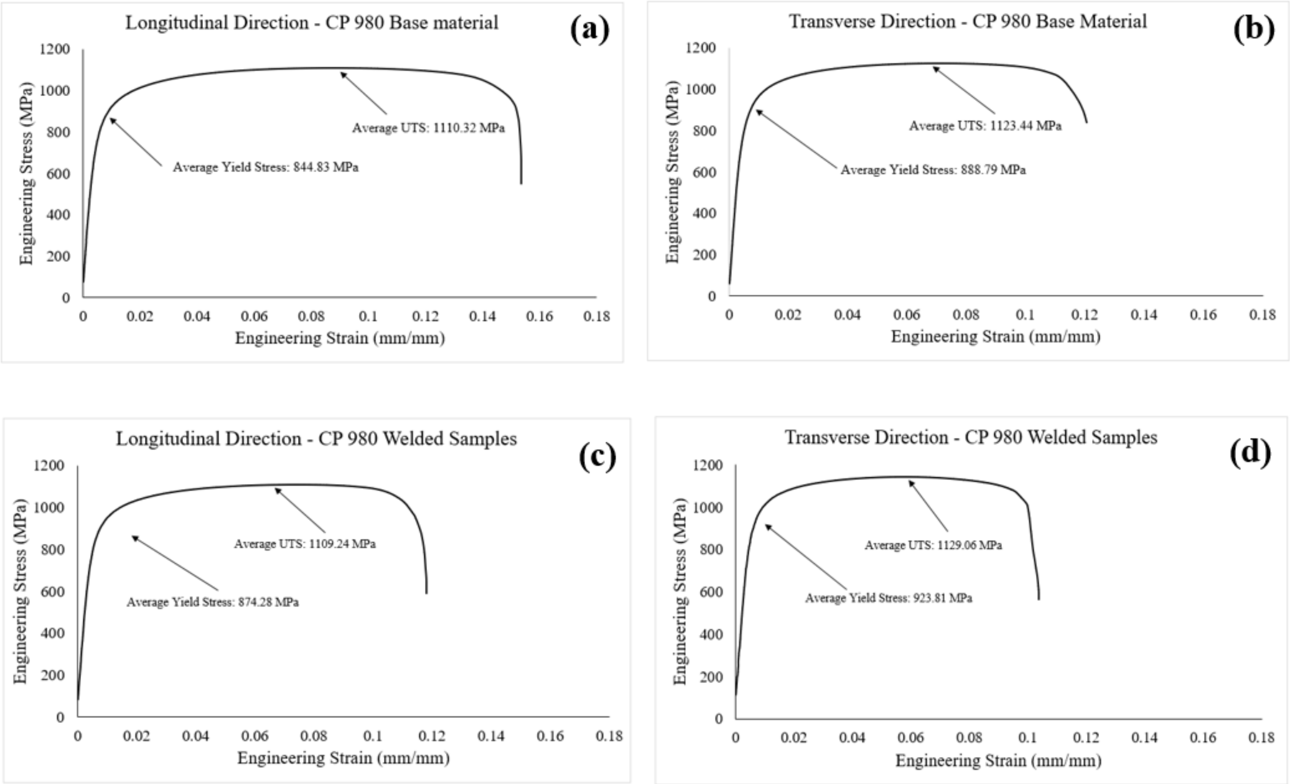

Figure 4.8: CP 980 Average Engineering Stress vs. Strain Graphs of Base Metal (Longitudinal (a) and Transverse directions(b)) and Welded Samples (Longitudinal (c) and Transverse Orientations (d)). The welded samples failed in the BM.

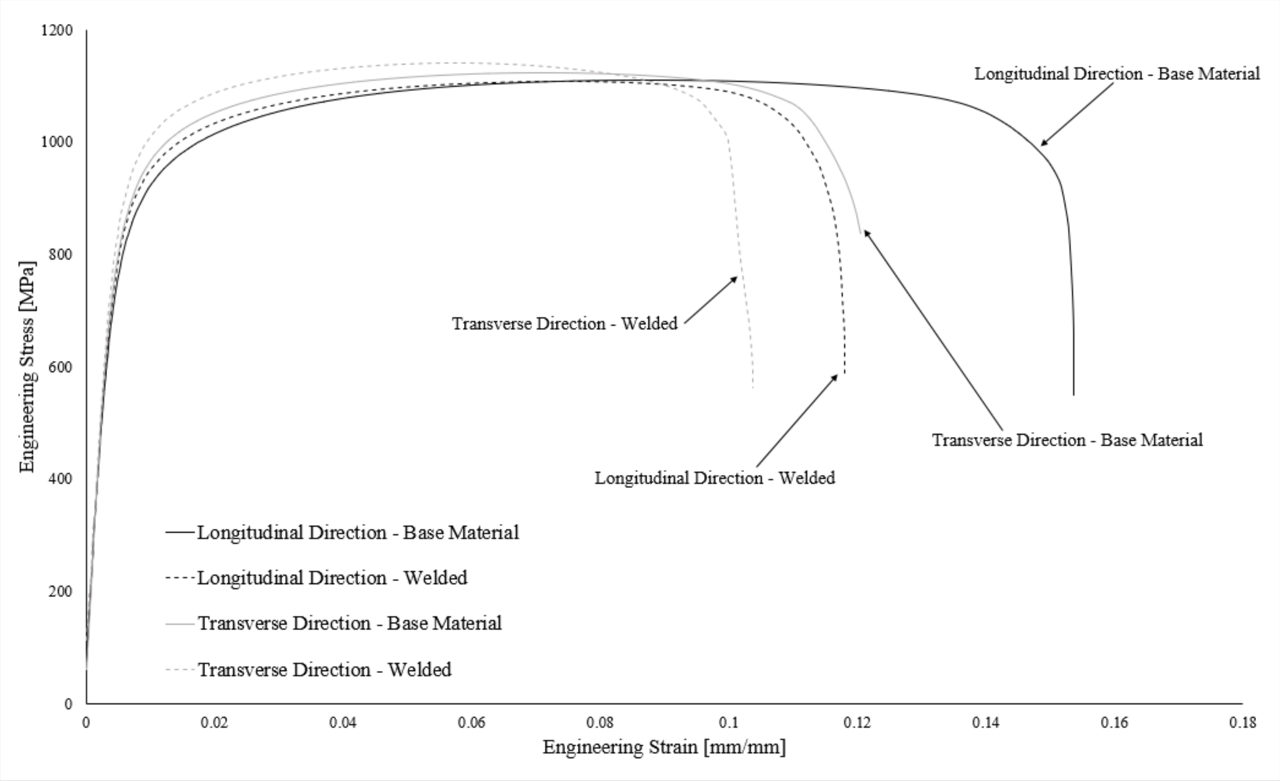

Figure 4.9: CP 980 Overlay of Average Engineering Stress vs. Strain Graphs of Base Metal (Longitudinal and Transverse directions) and Welded Samples (Longitudinal and Transverse Orientations).

4.2.1.2 HAZ Hardness Profile and Microstructure of CP 980 Steel

A hardness profile analysis - Figure 4.10 - was one of the methods used to understand the HAZ and the effects that the laser weld had on the base material microstructure. The weld hardness profile showed symmetry with respect to the centre of the weld. The weld profile shows hard and soft zones within the weld. The average hardness value of the BM was ~349 HV, the softest measurement within the HAZ was 297 HV, the hardest measurement in the HAZ was 519 HV and the average FZ hardness measurement was ~481 HV.

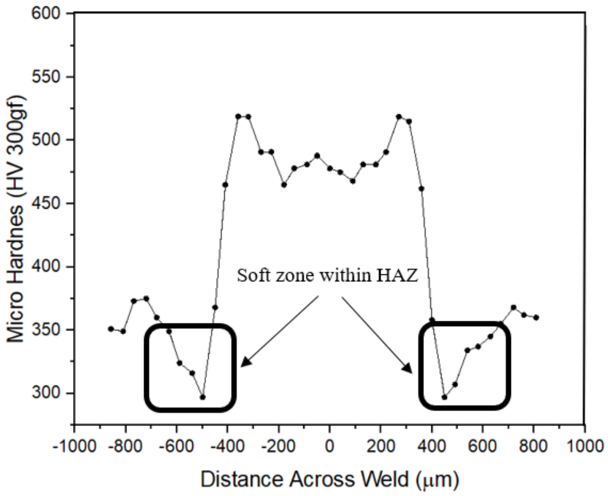

Figure 4.10: Microhardness Profile across the laser weld showing symmetry of the weld

The microstructures across the weld profile were analyzed and this analysis showed a distinct change in microstructure as the analysis moved from the FZ out towards the base metal as outlined in Figure 4.11. The FZ exhibited a large-grain martensite microstructure (See Figure 4.11 (a)), the UCHAZ exhibited a finer-grain martensite (See Figure 4.11 (b)), the ICHAZ exhibited a ferrite and martensite microstructure (See Figure 4.11 (c)), and the SCHAZ exhibited a ferrite, bainite and tempered martensite microstructure (See Figure 4.11 (d)). These zones are explained in Chapter 2, Section 2.2.1 and Chapter 5, Section 5.2. Figure 4.11 (e) is a magnified micrograph of the tempered martensite present in the SCHAZ.

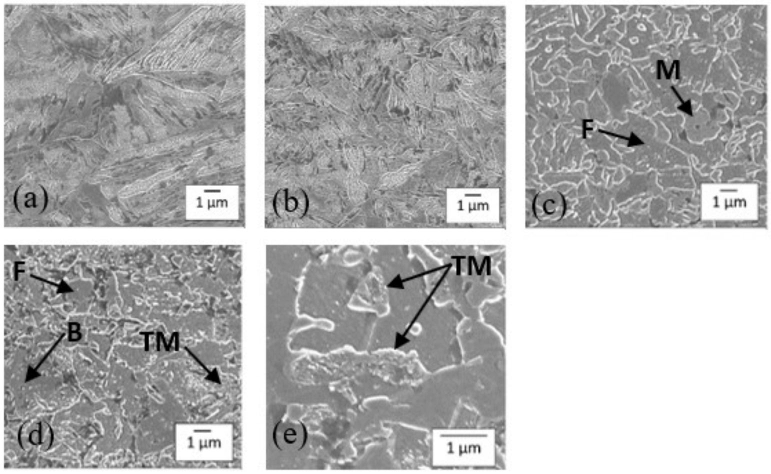

Figure 4.11:SEM micrographs showing the different microstructures within the CP 980 weld zone - a: FZ; b:UCHAZ, c: ICHAZ; d-e SCHAZ (M: Martensite; F: ferrite; B: bainite and TM: tempered martensite)

The weld hardness profile was approximated into various zones that correlated with the microstructures observed (see Figure 4.12). The different zone-widths were estimated using this information. The FZ was ~600µm, which is consistent with the laser beam spot diameter. The UCHAZ was ~50µm, the ICHAZ was ~100µm and the SCHAZ was ~225µm. Note that the soft zone is within the SCHAZ. The hard peaks on either side of the FZ were correlated to the UCHAZ where the martensite was fine-grain as compared to the large-grain martensite observed in the FZ.

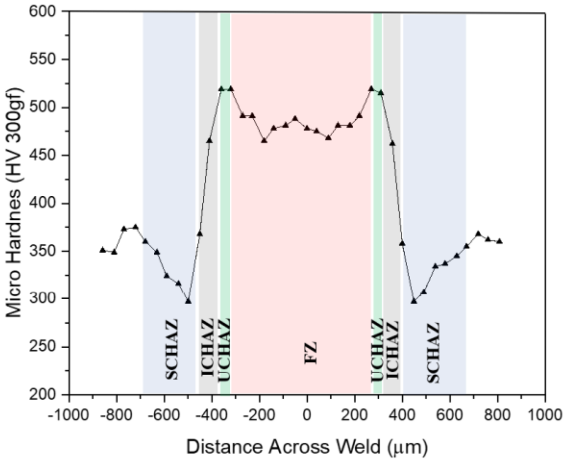

Figure 4.12:Weld Zone Microhardness Profile Showing 4 distinct Hardness Zones and their Respective Cross-section widths.

4.2.2 Hot Dipped Galvanealed (HDGA)DP 980

Figure 4.13 outlines the cross-sections of the welds produced at different laser powers and transverse speeds with the DP 980 steel. During welding it was observed that, for the 2kW and 3kW laser power level, as the transverse speed increased, the weld reached a point where the penetration became incomplete. This can be seen on the welds produced at 2kW-14, 2kW-16, 2kW-20m/minute and 3kW-20m/minute.

It was also observed that as the welding power increased, the tendency of the weld to exhibit concavity also increased due to vaporization of the material. The welds produced at 2kW showed little-to-no concavity. At 3kW, the welds started showing the presence of concavity. The concavity was more prevalent in the higher welding powers (4kW, 5kW and 6kW).

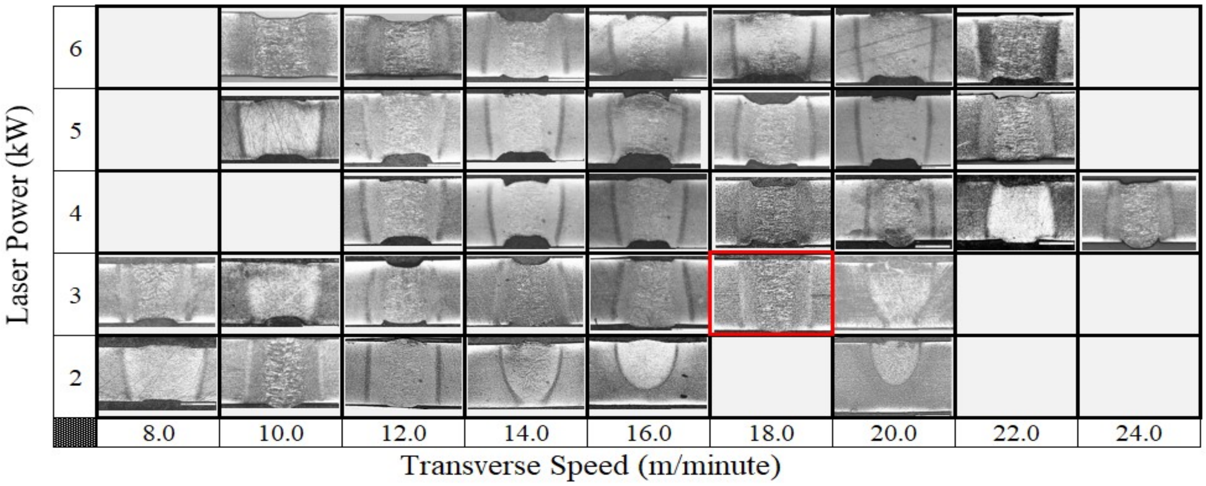

Figure 4.13: Weld cross-section charts showing different Laser Power vs. Transverse Speed combinations. The weld produced using 3 kW at 18m/minute (outlined in red) was chosen as the optimum weld (exhibiting full BM penetration with minimum concavity). This weld parameter combination was used for the remainder of the research with this material

Using the criteria outlined above in section 3.1, the weld that was produced with a welding power of 3kW and a transverse speed of 18m/s was chosen as the best weld and was used for the remainder of the research testing.

4.2.2.1 Mechanical Properties of Welded DP980 HDGA Material

To determine if the HAZ of the weld introduced detrimental effects on the overall performance of the joint, welded coupons were prepared for uniaxial tensile testing with welds positioned perpendicular, and parallel to the material's rolling direction. Aside from being able to compare the mechanical properties of the welded samples to the base material, the test was also used to determine where the tensile failure occurred. On the samples welded with 3kW and 18m/s, the failures occurred in the weld zone. This was different than the observations seen in the CP 980 steel in Phase 1.

Figures 4.14 shows the individual engineering and true stress-strain graphs for the base metal and the samples welded with the different weld orientations. The longitudinal direction implies that the rolling direction is parallel to the tensile specimen axis and the transverse directions implies that the rolling direction is 90° to the tensile specimen. In all cases, the welds are always perpendicular to the axis of the specimen – see Figure 3.2. For comparison purposes, Figure 4.15 combines Figures 4.14 (a)-(d) onto one plot. The tensile tests showed a decrease in total elongation on the welded samples – in both weld orientations. In all cases the tensile tests showed a decrease in total elongation on the welded samples. The yield strengths and tensile strengths were similar for all the samples.

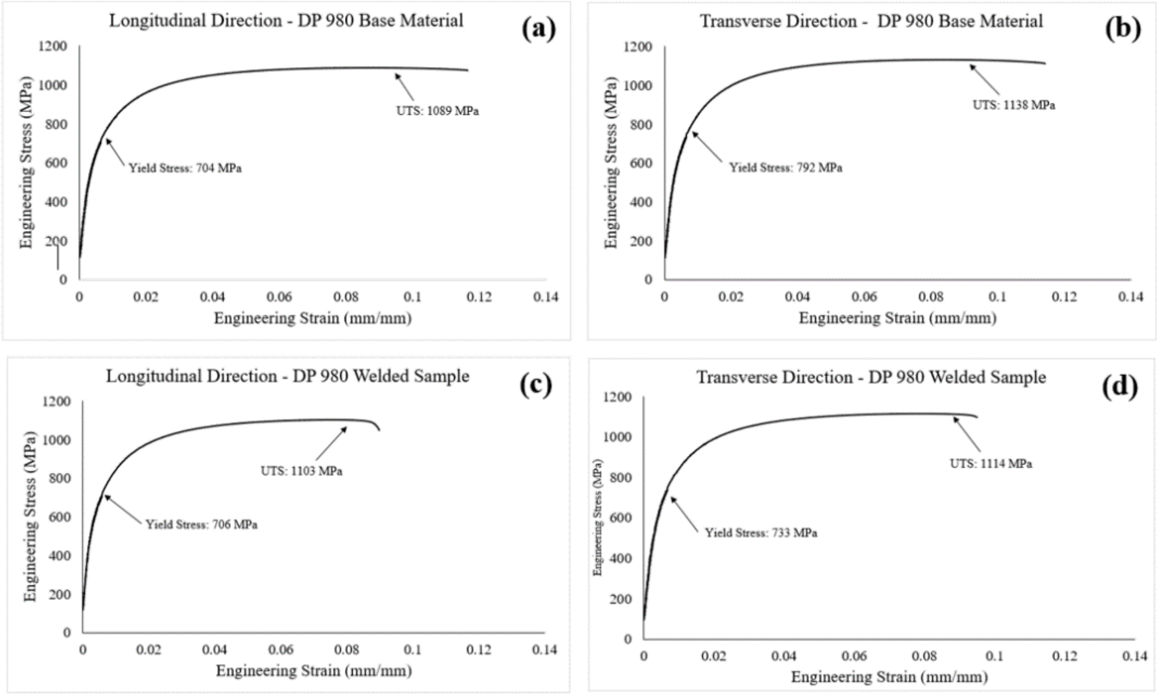

Figure 4.14: DP 980 Engineering Stress vs. Strain Graphs of Base Metal (Longitudinal (a) and Transverse directions(b)) and Welded Samples (Longitudinal (c) and Transverse Orientations (d)). The welded samples failed in the Weld HAZ

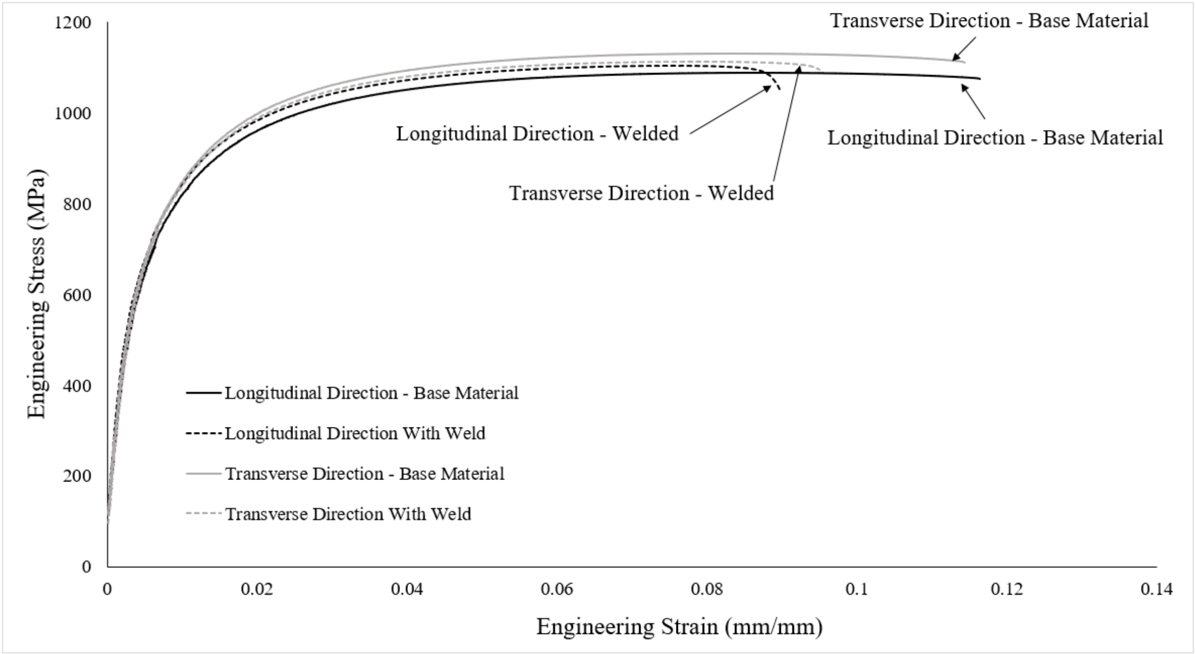

Figure 4.15: DP 980 Overlay of Engineering Stress vs. Strain Graphs of Base Metal (Longitudinal and Transverse directions) and Welded Samples (Longitudinal and Transverse Orientations).

4.2.2.2 Weld Characterization – HAZ Hardness Profile and Microstructure of DP980 HDGA

A hardness profile analysis - Figure 4.16 - was one of the methods used to understand the HAZ and the effects that the laser weld had on the base metal microstructure. The weld hardness profile showed symmetry with respect to the centre of the weld. The weld profile shows hard and soft zones within the weld. The average hardness value of the BM was ~345 HV, the softest measurement within the HAZ was 305 HV and the average FZ hardness measurement was ~461 HV.

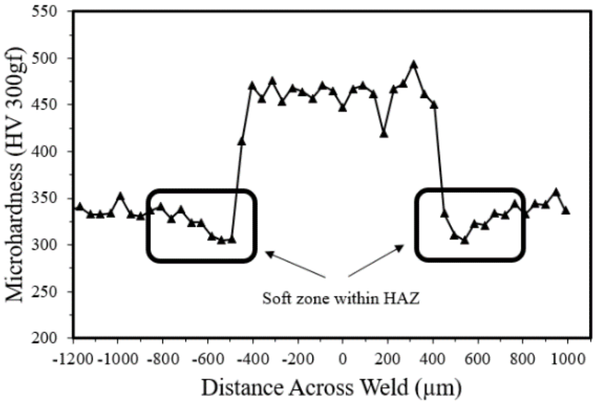

Figure 4.16: Microhardness Profile across the laser weld showing symmetry

The microstructures across the weld profile were analyzed and this analysis showed a distinct change in microstructure as the analysis moved from the FZ out towards the base metal– outlined in Figure 4.17. The FZ exhibited a large-grain martensite microstructure - Figure 4.17 (a), the UCHAZ exhibited a finer-grain martensite microstructure - Figure 4.71 (b), the ICHAZ exhibited a ferrite and martensite microstructure – Figure 4.17 (c), and the SCHAZ exhibited a ferrite, and tempered martensite microstructure. These zones are explained in Chapter 2, Section 2.2.1 and

Chapter 5, Section 5.2. Figure 4.17 (e) is a magnified micrograph of the tempered martensite and ferrite present in the SCHAZ.

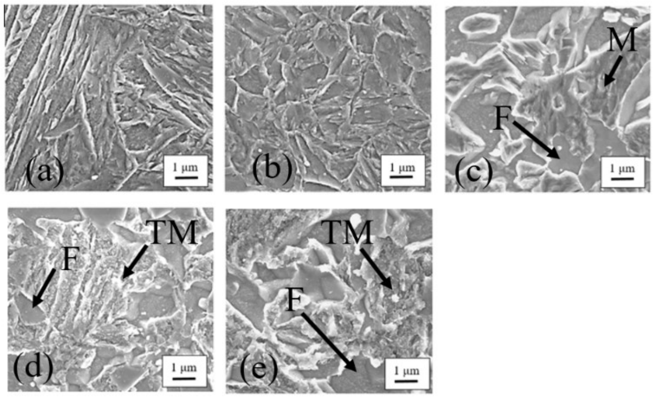

Figure 4.17: SEM micrographs showing the different microstructures within the DP 980 weld zone - a: FZ; b:UCHAZ, c: ICHAZ; d-e SCHAZ (M: martensite; F: ferrite; and TM: tempered martensite)

The weld hardness profile was divided into the zones that correlated with the microstructures observed - Figure 4.18. The different zone widths were approximated using this information. The (FZ) was ~600µm, which is consistent with the laser beam spot diameter. The UCHAZ was ~100µm, the ICHAZ was ~75µm and the SCHAZ was ~300µm.

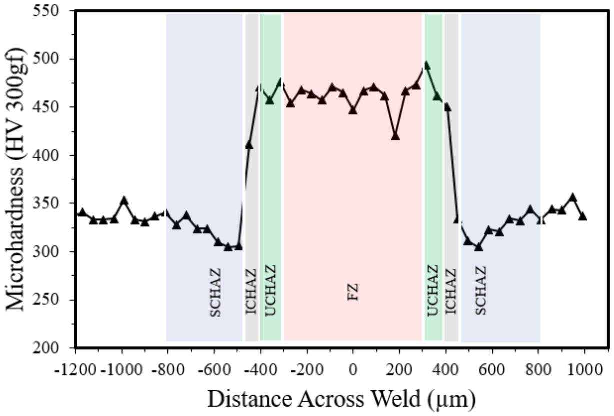

Figure 4.18:Weld Zone Microhardness Profile Showing 4 distinct Hardness Zones and their Respective Cross-section widths.

4.3 Formability Performance of Welded Samples

4.3.1 Formability of Cold Rolled, Uncoated CP 980 material

4.3.1.1 Global Formability and Local Formability of CP 980 Welded Material

The LDH tests showed a reduction in punch height on all the welded samples - as compared to the LDH of the base metal. Figure 3.3 (a)-(e) shows the weld layouts and offsets used in these formability tests. This layout method was used to balance the strain on either side of the hemispherical forming punch during the global formability tests. The data showed that as the weld-offset distance decreased, the punch height also decreased. It was also observed that the direction of the welds – with respect to the material's rolling direction (longitudinal vs. transverse) – had little-to-no effect on the LDH performance. The longitudinal direction is parallel to the material's rolling direction and the transverse direction is perpendicular to the material's rolling direction. Figure 4.19 shows the average punch height trend of the base material vs. the different weld offsets. The data suggests that the welds located greater than 25mm from the forming punch's center line had a minimum effect on the forming performance of the sample.

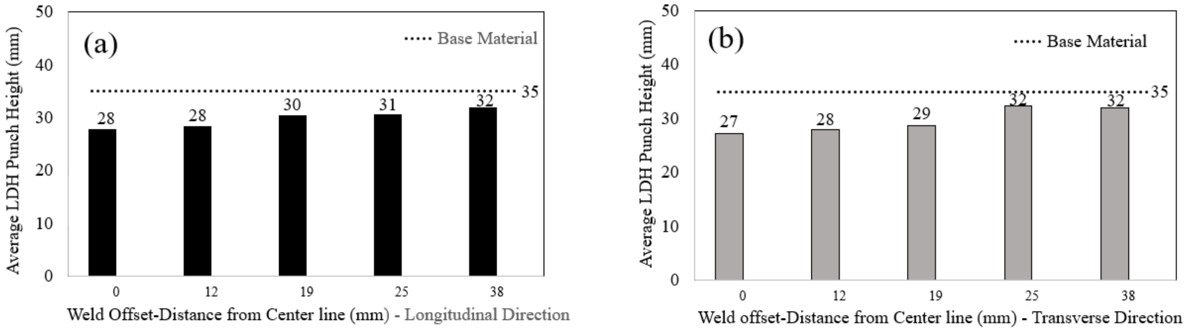

Figure 4.19: CP 980 LDH results comparing welded samples to the BM: (a) represents data from samples with welds that were parallel to the material's longitudinal direction and (b) represents data from samples with welds that were parallel to the material's transverse direction. In both graphs, the dotted line represents the average LDH punch height of the BM.

Using samples with the same weld layout and center line offsets as the LDH tests, major and minor strains were measured using DIC during bi-axial stretch forming. Figure 4.20 (a) and (c) show the major and minor strain values in the samples with the welds in the longitudinal direction and Figure 4.20 (b) and (d) show the major and minor strain values in the samples with the welds in the transverse direction. In all cases, at failure, the strain values at the weld locations were less than the strain measured at the same locations within the base metal at failure. They also show a consistency in the amount of bi-axial strain that the weld could experience before failure.

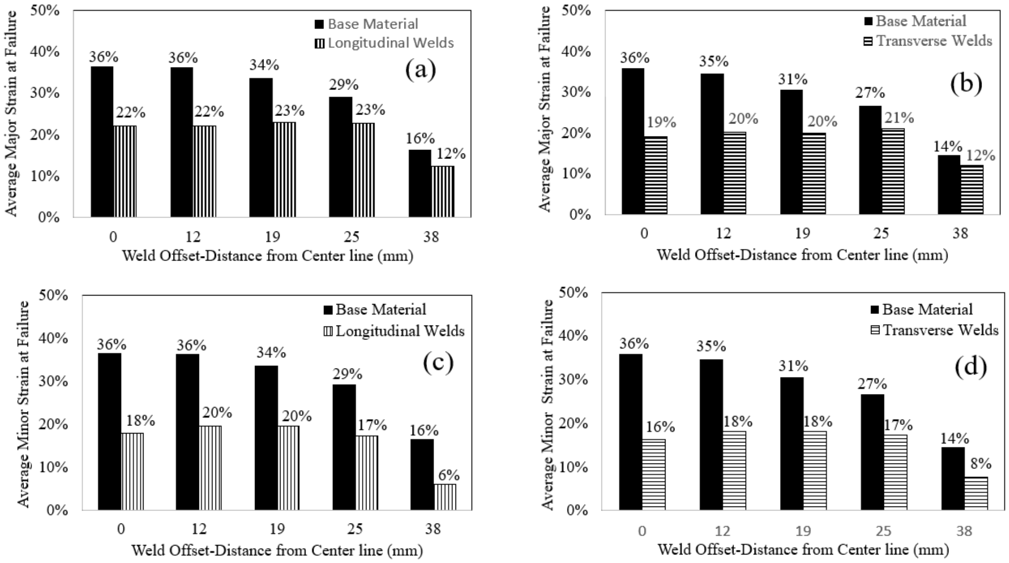

Figure 4.20: CP 980 strain analyses during bi-axial stretch testing. (a) & (b) represent major strain with longitudinal and transverse welds respectively and (c) & (d) represent minor strain with longitudinal and transverse welds respectively.

Figure 4.21 is an example of the major-strain values measured across the welded sample with a 12mm offset just before failure. A decrease in strain at the weld locations can be seen which was caused by the presence of the weld. A decrease in strain was also seen at the center of the sample which was the result of friction between the material and the forming punch during forming.

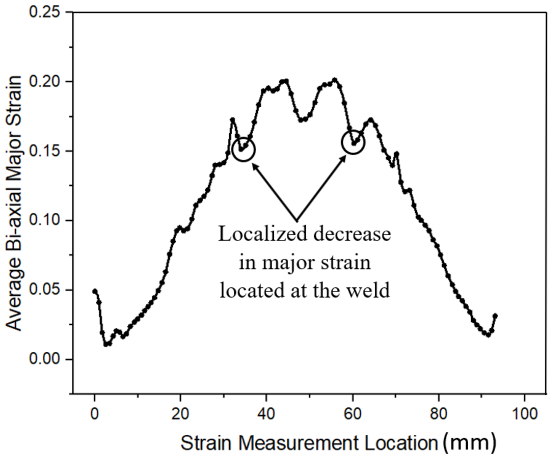

Figure 4.21: Major strain values during bi-axial stretch testing on a sample with 12mm offset welds oriented in the transverse direction. Strain values were measured across the sample, perpendicular to the welds, and show a decrease in strain at the welds.

The welded-sample LDH data was used to determine the strain distribution of the base metal where the forming punch was at the same height as when the welded sample failed. When this strain data was overlaid with the welded sample data, the strain distribution difference becomes obvious. Figure 4.22 is an example of the strain-data-overlay highlighting how the material flow looks to be restrained at the location of the weld.

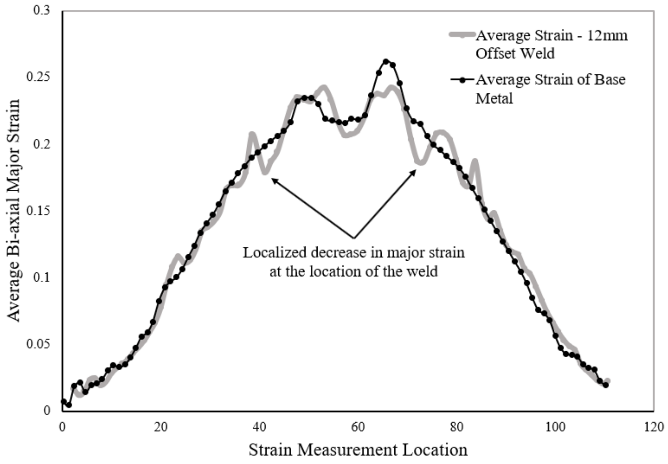

Figure 4.22: Major strain values during bi-axial stretch testing on a sample with 12mm offset welds and the base metal at the same LDH punch height. This overlay comparison visually shows a decrease in strain at the welds.

DIC images captured during forming confirmed that the failures on the samples with weld offsets of 0mm (centre line), 12mm, 19mm and 25mm initiated at the weld during the bi-axial stretch tests. At these locations, the major and minor strain values were similar on all the tests as outlined in Figure 4.20 (a-d). The strain-data outlier was with the 38mm offset welds. This implies that, for these specific samples, the failure initiated in the base metal and not at the welds.

During the LDH and bi-axial global formability tests, all samples experienced the same failure trend. The crack propagated across the top of the dome, in a direction perpendicular to the welds i.e. the direction of the failure happened regardless of the orientation of the weld with respect to the material's RD. When BM samples were tested, the failure initiated at the centre of the punch and propagated in the material's RD. Figure 4.23 shows the different weld samples and highlights the consistent failure direction.

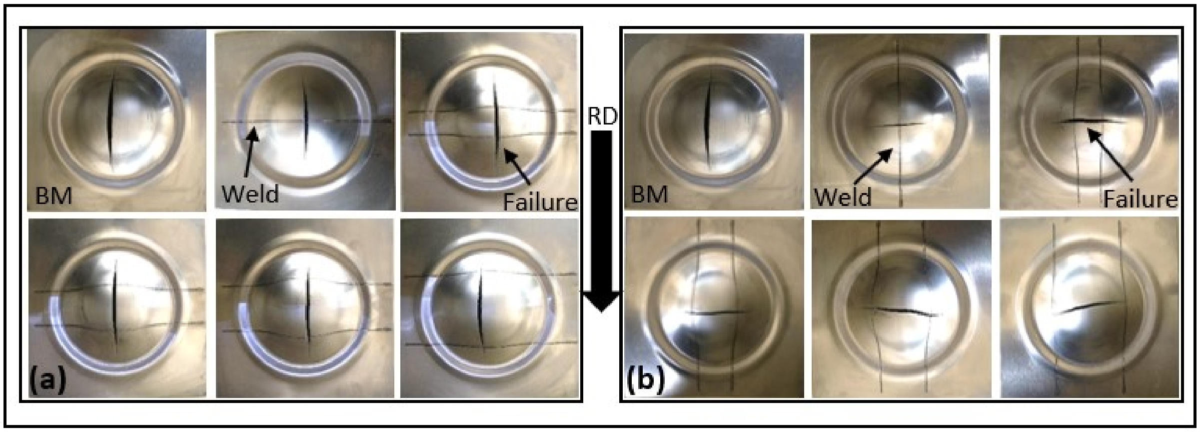

Figure 4.23: Global formability samples (LDH and Bi-axial stretch test) showing that the failure direction was perpendicular to the welds: (a) shows the samples with welds in the material's transverse direction and (b) shows the samples with welds in the material's longitudinal direction

When the welded sample's local formability was tested by hole expansion, the average λ decreased from 30% (BM) to 21% (welded samples). Figure 4.24 shows the top surface (a) and side profile

(b) of a formed hole expansion sample. It was observed that failures initiated in the HAZ of the weld oriented parallel to the rolling direction. The failure travelled along the weld HAZ as shown in Figure 4.24 (c).

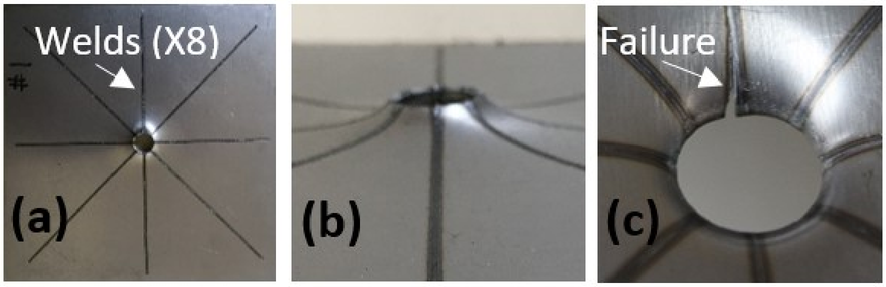

Figure 4.24: *HET samples after forming (a)-top surface, (b) - side profile. (c) highlights the failure propagating along the weld (running in the longitudinal direction)*

4.3.2 Formability of HDGA DP 980 material

4.3.2.1 Global Formability and Local Formability of DP 980 Welded Material

The LDH tests showed a reduction in punch height on all the welded samples - as compared to the LDH of the base metal. Figure 3.3 (a)-(e) shows the weld layouts and offsets used in these formability tests. This layout method was used to balance the strain on either side of the hemispherical forming punch during the global formability tests. The longitudinal direction is parallel to the material's rolling direction and the transverse direction is perpendicular to the material's rolling direction. The data showed that as the weld-offset distance decreased, the punch height also decreased. It also shows that at 25mm and 38mm weld offsets, the LDH performance was similar to that of the BM. This suggests that the effects of the welds were more significant at distances equal to, or less than, 19mm from each other. Figure 4.25 shows the punch height trend and that the direction of the welds (longitudinal vs. transverse) had little-to-no effect on the LDH performance.

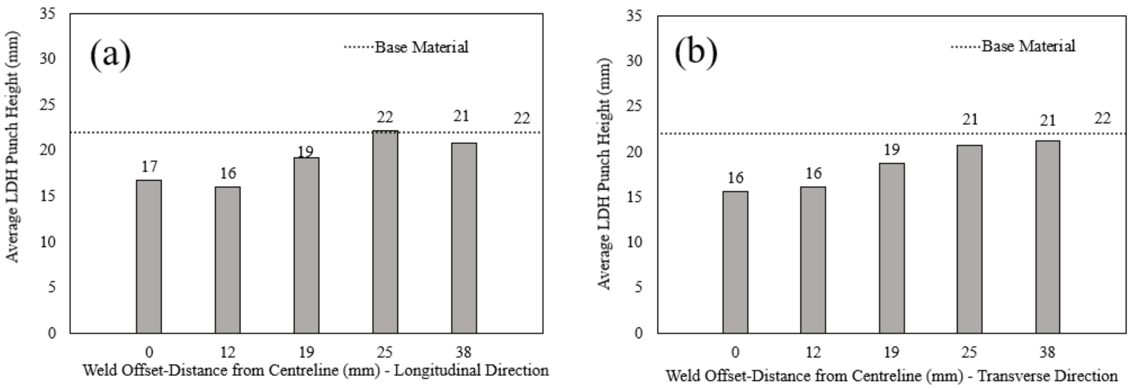

Figure 4.25: DP 980 LDH results comparing welded samples to the BM: (a) represents data from samples with welds that were in the longitudinal direction and (b) represents data from samples with welds in the transverse direction. In both graphs, the dotted line represents the LDH punch height of the BM.

Using samples with the same weld layout and center line offsets as the LDH tests, major and minor strains were measured using DIC during bi-axial stretch forming. Figure 4.26 (a) and (c) show the major and minor strain values in the samples with the welds in the longitudinal direction and Figure 4.26 (b) and (d) show the major and minor strain values in the samples with the welds in the transverse direction. Figure 4.26 shows that, when failure occurred, the major and minor strain values at the weld locations were less than the strain measured at the same locations within the BM only on the samples with the weld offsets of 0 and 12mm. This was compared to the strain values measured at 19mm, which shows a marginal decrease in strain before failure. The strain values at 12mm and 38mm offsets were the same for the welded samples and the base metal. Figure 4.26 also shows a consistency in the amount of bi-axial strain that the weld could experience before failure.

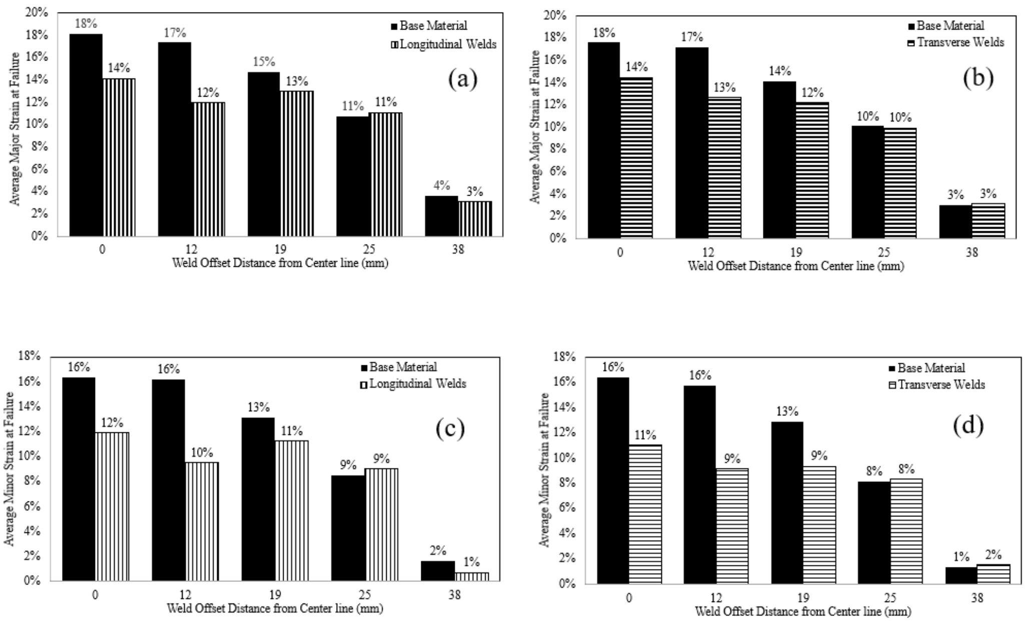

Figure 4.26: DP 980 strain analysis during bi-axial stretch testing. (a) & (b) represent major strain with longitudinal and transverse welds respectively and (c) & (d) represent minor strain with longitudinal and transverse welds respectively.

Figure 4.27 is an example of the major-strain values measured across the welded sample with a 12mm offset just before failure. An increase in strain at the weld locations can be seen which was caused by the presence of the weld.

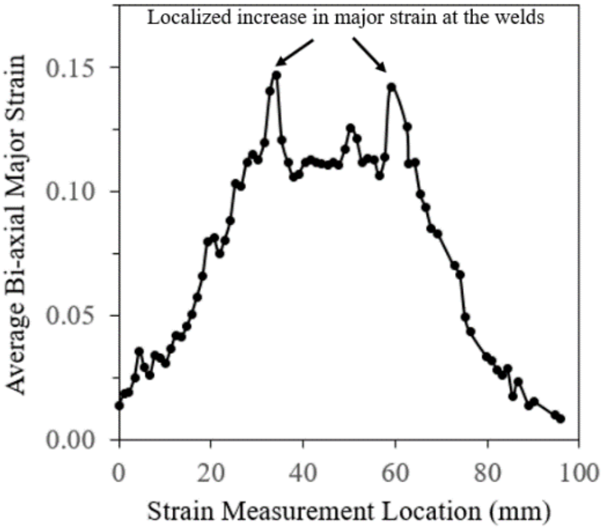

Figure 4.27 Major strain values during bi-axial stretch testing on a sample with 12mm offset welds oriented in the transverse direction. Strain values were measured across the sample, perpendicular to the welds, and show a decrease in strain at the welds.

The welded-sample LDH data was used to determine the strain distribution of the BM where the forming punch was at the same height as when the welded sample failed. When this strain data was overlaid with the welded sample data, the strain distribution difference becomes obvious. Figure 4.28 is an example of the strain-data-overlay highlighting how the material flow looks to increase at the location of the weld.

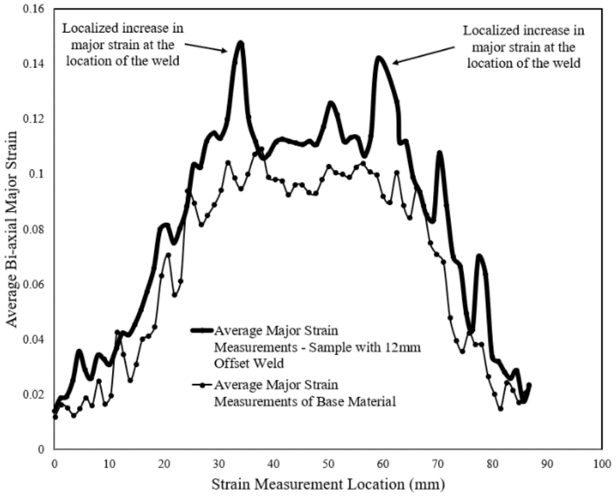

Figure 4.28: Major strain values during bi-axial stretch testing on a sample with 12mm offset welds and the base metal at the same LDH punch height. This overlay comparison visually shows an increase in strain at the welds.

During the LDH and bi-axial global formability tests, the samples with a weld offset equal-to-or-less-than 19mm experienced the same failure trend. The crack propagated along the weld regardless of the weld's orientation - with respect to the material's RD. When the weld offset was greater than 19mm, the samples failed the same way the base metal failed – across the nose of the forming punch with the crack propagating in the material's rolling direction. When base metal samples were tested, the failure initiated at the centre of the punch and propagated in the material's RD. Figure 4.33 shows the different weld samples and the failure direction.

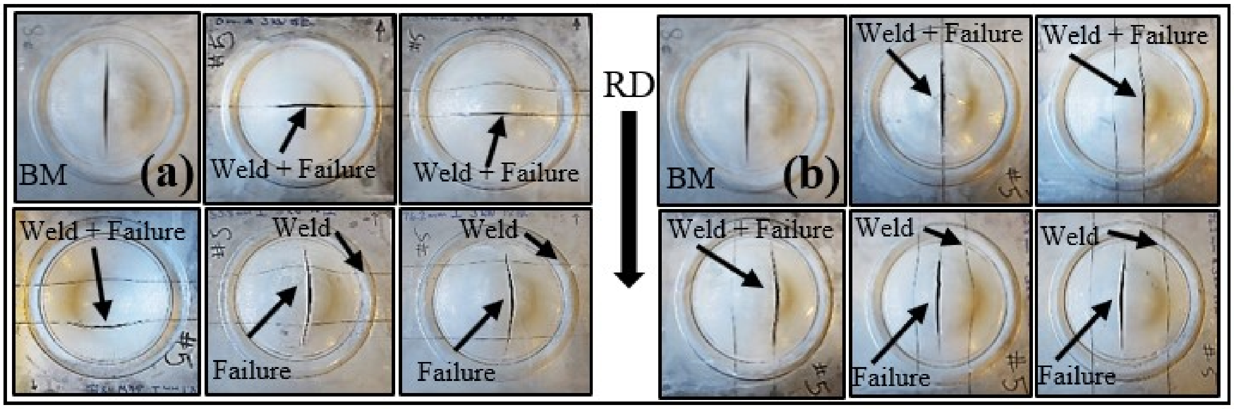

Figure 4.29: Global formability samples (LDH and Bi-axial stretch test) showing that the failure direction was parallel to the welds: (a) shows the samples with welds in the material's transverse direction and (b) shows the samples with welds in the material's longitudinal direction

When the welded sample's local formability was tested by hole expansion, the average λ decreased from 11% (base metal) to 9% (welded samples). Figure 4.30 shows the top surface (a) and side profile (b) of a formed hole expansion sample. It was observed that failures initiated in base material and propagated in a random direction – with respect to the material's rolling direction which can be seen in Figure 4.30 (c).

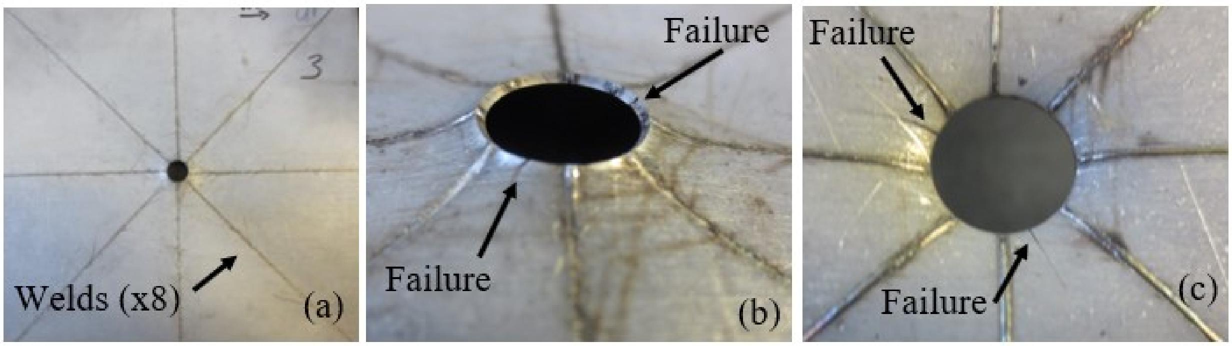

Figure 4.30: HET samples after forming (a)-top surface, (b) - side profile. (c) highlights the failure initiated and propagated in the base material. The failure direction did not favor a direction related to the material's rolling direction.

Chapter 5

5.0 Discussion

5.1 Characterization of CP 980 and DP 980 Base materials

When comparing the two base metals, the first difference was seen with the chemistry. The CP 980 has more Carbon and Silicon and less Manganese and Chrome + Molybdenum compared to the DP 980 as outlined in Table 5.1.

Table 5.1: Chemistry comparison between the CP 980 material and DP 980 material

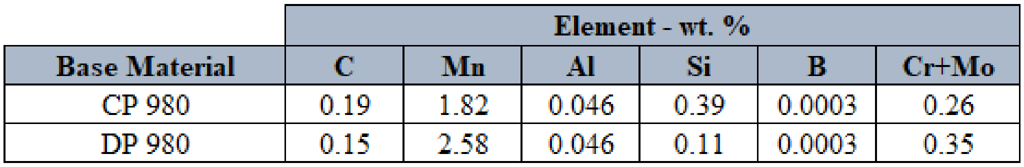

	Element - wt. %					
Base Material	**C**	**Mn**	**Al**	**Si**	**B**	**Cr+Mo**
CP 980	0.19	1.82	0.046	0.39	0.0003	0.26
DP 980	0.15	2.58	0.046	0.11	0.0003	0.35

One significant factor that determines the composition strategy is the different heating and cooling capabilities of the processing line. The compositions for these steels were each developed for their intended process path – either a continuous galvanizing line (DP steel) or a continuous anneal line (CP steel). Because these alloying elements affect the base metal microstructure development, it also affects how the material will react to the local thermal cycle which it is exposed to during a welding process.

As explained in Eq. 2.1 & 2.2, each steel will have a different inter-critical zone with respect to the Fe-Fe_3C phase diagram. They will also have different *Continuous Cooling Transformation*

(CCT) diagrams as Carbon, Manganese, Chromium and Silicon influence the start temperatures of martensite and/or bainite.

The mechanical properties of the two materials are outlined in Table 5.2. Note that the longitudinal-direction mechanical properties refer to the properties which are parallel to the steel's rolling direction and the transverse-direction mechanical properties refer to the properties which are 90° to the rolling direction.

Table 5.2: Mechanical Property Comparison between the CP 980 material and DP 980 material

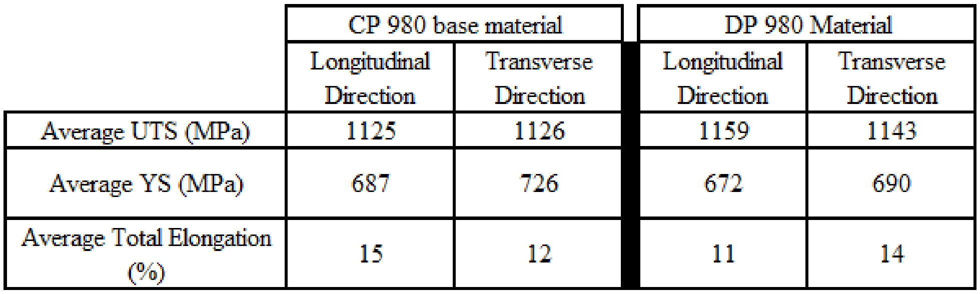

	CP 980 base material		DP 980 Material	
	Longitudinal Direction	Transverse Direction	Longitudinal Direction	Transverse Direction
Average UTS (MPa)	1125	1126	1159	1143
Average YS (MPa)	687	726	672	690
Average Total Elongation (%)	15	12	11	14

These materials were designed to meet minimum mechanical property values in the transverse direction which were: tensile strength of 980 MPa, yield strength of 590 MPa and, total elongation of 12 % - which both steels satisfied. There was a difference in anisotropy between the CP and DP steels. The CP steel had the same tensile strength in both the longitudinal and transverse directions where the DP steel had a 16 MPa difference between the two directions. With respect to the material's yield strength, the CP steel had a 39 MPa difference between the two directions where the DP steel had only 18 MPa. Besides the fact that one material was coated and the other was not, both steels can be classified as 980 AHSS grade based on their mechanical properties.

A point of discussion surrounds the tensile strength of the DP steel, which was well above the 980 MPa minimum and was also higher than the CP steel. Since DP steels gain their strength through the volume fraction of martensite [4], this steel would contain more martensite and less ferrite than other steels of the same grade if their tensile strength was closer to the 980MPa minimum value. The effects of this high strength will be evident when the material's formability performance is reviewed.

A significant difference between the two steels studied was seen when their microstructures were analyzed. The CP980 steel - processed on the continuous annealing line – had three microconstituents: bainite, martensite and ferrite. Bainite had the largest volume fraction at 41%, followed by martensite at 32% and ferrite at 27%. The DP 980 steel – processed on a continuous galvanizing line – had two microconstituents: martensite and ferrite. Martensite made up 66% of the volume fraction with the remainder being ferrite at 34%. The presence of these phases within each of these two grades of steel aligns with industry expectations. The microstructures of the CP 980 and DP steels are outlined in Figure 4.1 and Figure 4.4 respectively.

One of the perceived advantages of DP steels is that they have good global formability due to the presence of ferrite within its microstructure [3]. During this study, it was predicted that the DP steel would have similar, or better, global formability performance as the CP material. The average LHD of the CP steel was 35mm as compared to 22mm seen with the DP. The formability of the DP material represented ~37% decrease in punch height - which can be seen in Figure 5.1. In this study, the specific CP steel appears to have better global formability as compared to the specific DP steel. When the n-values – taken from the longitudinal-direction true stress vs. true strain data – were compared, the CP steel had an n-value of 0.113 and the DP material had an n-value of 0.105, confirming that the CP steel would have a superior global formability. This decrease in n-value can be attributed to the microstructure of the DP steel. Since strain is distributed through the soft ferrite phase, and there was only 34% ferrite in the volume fraction of the DP steel, the global formability would be negatively impacted by the high percentage of martensite.

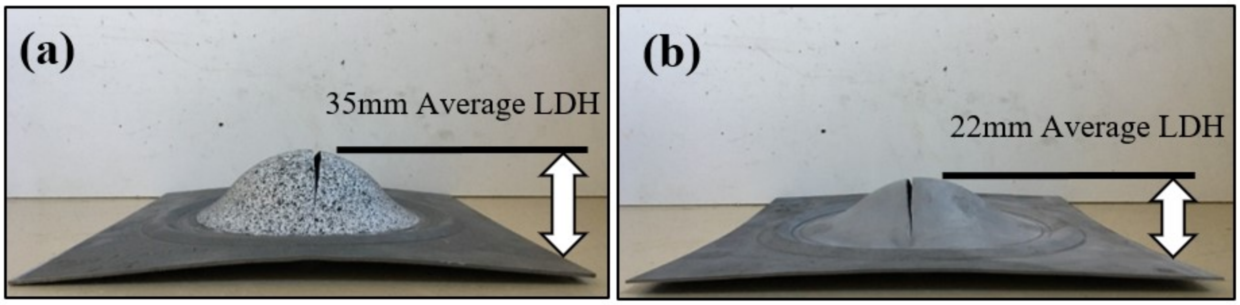

Figure 5.1: LDH test samples showing the difference in performance between the 2 base materials which had similar mechanical properties: a) CP material, b) DP material

The global formability strain distribution analysis showed a considerable decrease in the bi-axial strain that the DP steel could be exposed to before failure. A major strain data overlay of the DP and CP base metals is shown in Figure 5.2.

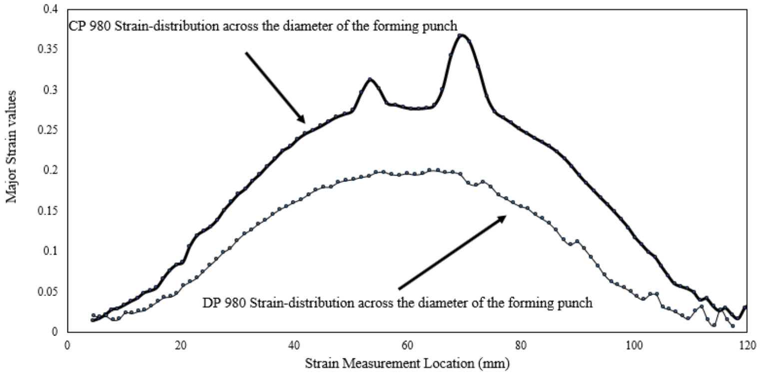

Figure 5.2: Example of Major-Strain measurement distribution across the punch for the CP and DP steels showing a significant difference in bi-axial stretch performance. Measurements were taken at the point of material failure.

The global formability performance of the DP base metal could be explained by reviewing the mechanical properties and microstructure. As mentioned above, the tensile strength of the DP steel was well above the minimum requirement and it was higher than the CP steel's tensile strength. The strength of DP steels is related to the percentage of the martensite present in the microstructure [4]. The phase volume analysis showed that the microstructure was made up of ~66% martensite and ~34% ferrite. Since strain is distributed through the ferrite phase, the additional martensite associated with the tensile strength would be detrimental to the global formability of this material. This was also seen in the LDH tests performed.

Local formability also showed a significant difference between the two grades of steel. CP steels are known for having higher yield strengths than DP steels along with better flanging (edge stretch) performance [3], [4], [6]. The average hole expansion (λ) for the CP steel was 30% and the average λ for the DP material was 11%. This difference was predictable as previous studies have highlighted that the CP microstructure performs better in hole expansion tests. This performance is related to the presence of bainite in the CP microstructure [23], [48] as it acts as an intermediary-strength phase between the soft ferrite and the hard martensite phases. The DP microstructure only contained a hard phase (martensite) and a soft phase (ferrite). Studies have shown that AHSS containing bainite exhibits a significant increase in λ as compared to AHSS of the same minimum tensile strength with a microstructure of martensite and ferrite [24].

5.2 Differences Between the CP 980 and DP 980 Weld Joints

Energy per unit area of the weld was calculated and used to compare the different welding set-ups for each material – see Eq.5.1

$$Energy\ per\ Unit\ Weld\ Area\ (\frac{KJ}{mm3}) = \frac{Laser\ Power\ (kW)}{Linear\ Speed\ \left(\frac{mm}{minute}\right)*sheet\ thickness(mm)*weld\ width(mm)}*60 \qquad \text{(Eq. 5.1)}$$

The energy per unit area of weld was $2.2\text{x}10^{-4}$ kJ/mm^3 for the HDGA DP 980 steel and $1.7\text{x}10^{-4}$ kJ/mm^3 for the CP 980. It took 30% less energy per unit area to produce an acceptable weld in the CP 980 steel which was 60% thicker (1mm thick DP 980 HDGA material vs. 1.6mm thick CP 980 CAL). It has been shown that when laser welding zinc coated steel, the laser vaporizes the zinc, creating a plasma cloud above the top surface of the workpiece [29]. This plasma cloud absorbs the laser beam which lowers the power density of the laser, requiring additional power to produce an acceptable weld [29].

Welding can be categorized as a non-isothermal heat treatment process due to the rapid heating and cooling of the base metal. The differences in the base metal's chemistry and initial microstructure would have affected the microstructures developed in the HAZ which is transferred to the hardness profile of the weld.

Figure 5.3 is a side-by-side comparison of the hardness profiles and corresponding HAZ sub-zones seen in the CP and DP welds. The FZ of both steels had comparable hardness values – between 450 and 475 HV. During SEM analyses, these areas both showed a 100% martensite microstructure as outlined in Chapter 4 Figures 4.13 (a) - CP material - and 4.21 (a) – DP material. This would have been the result of the material solidifying from the liquidous temperature at a very fast cooling rate.

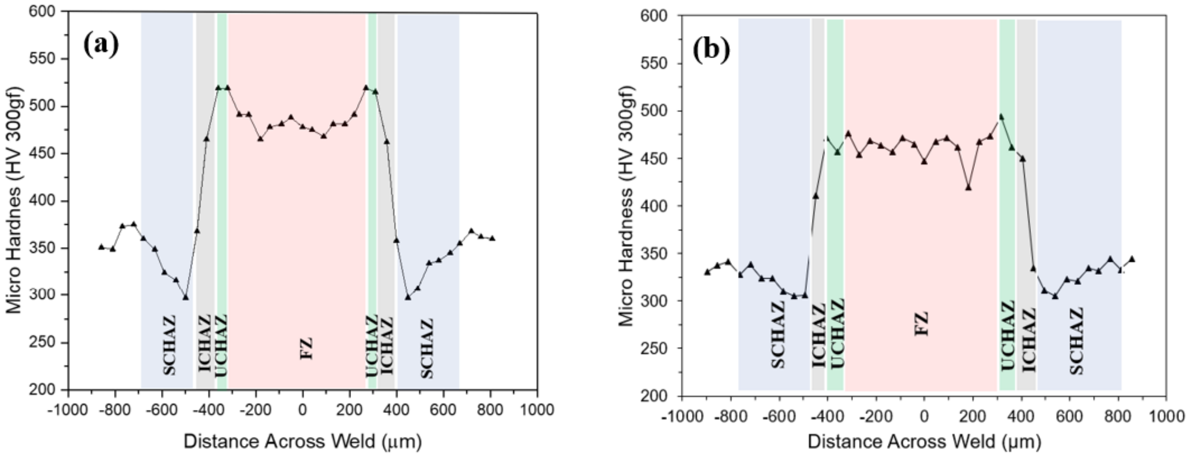

Figure 5.3: Weld Hardness Profiles and corresponding HAZ Sub-zones seen in the welded CP (a) and DP (b) steels

The zone immediately adjacent to the FZ was labelled the upper critical HAZ (UCHAZ). In the UCHAZ, the temperature of the weld would have ranged between the material's critical *Ac_3* and the liquidous temperature, resulting in a finer martensitic microstructure in both steels. This fine-grain microstructure was due to limited grain-size growth caused by the short time period that the steel was in the austenite region. The size of the austenite grains is directly tied to the size of the finished martensite grain size.

The zone immediately adjacent to the UCHAZ was labelled as the inter-critical HAZ (ICHAZ). This narrow-width band reflected the region where the temperature of the material reached values between the material's *Ac_1* and *Ac_3* critical temperatures. During the heating portion of the weld cycle, the microstructure is a combination of ferrite and austenite; however, during rapid cooling, the austenite transforms into martensite, creating a dual phase microstructure (ferrite and martensite). It was also noted that, in the CP steel, there was an absence of bainite in this zone, which was the dominant microstructure of the base metal. This would be the result of the rapid cooling which have missed the bainite area within the CCT diagram.

The soft zones of the hardness profile were the areas of the HAZ located between the ICHAZ and the base metal. These soft zone observations were predictable as many researchers have documented this phenomenon [10], [37], [38], [40], [42], [49]. The CP steel exhibited a smaller soft zone (~225µm) as compared to the DP steel's soft zone (~300µm). The soft zones would be the areas classified as the sub-critical HAZ (SCHAZ). The heat induced in SCHAZ (lower than critical Ac_1 temperature) tempers the martensite by allowing carbon from the unstable martensite to diffuse into the surrounding matrix, creating carbides [10]. Properties of the tempered martensite are related to the tempering temperature and the exposure time. Since the strength of martensite is directly proportional to its carbon content [4], diffusion causes the strength of the tempered martensite to be less than the original martensite. It has been seen that a non-isothermal cycle has a different tempering effect on martensite as compared to an isothermal heat treatment [49]. The rapid thermal cycle causes fine carbides to precipitate from the martensite but does not allow the martensite to reach the fourth stage of tempering [49]. The fourth stage of tempering includes the coarsening of the precipitated Fe_3C which eventually become spheroidised [50]. The softest location of the SCHAZ reflects the highest temperature the base metal is exposed to without exceeding the Ac_1 boundary

The effects of tempering on bainite is not as severe as compared to tempering martensite [50]. This can be explained by the fact that the carbon within bainite has been precipitated out as carbides [50], [51]. Un-tempered bainite is tougher and more ductile than tempered martensite [52]. It has been seen that when bainite is exposed to the rapid tempering temperatures seen in welding, it can decompose into different carbides, causing secondary hardening between the soft zone and the unaffected BM [53]. This phenomenon can be seen on the weld hardness profile of the CP steel.

There is an increase in hardness of the HAZ as the profile moves out of the soft zone towards the base metal.

The tempering effects of martensite and bainite can explain why the soft zone is wider in the DP steel as compared to the CP steel. The microstructure of the DP steel was made up of 66% martensite and contained no bainite. In comparison, the CP steel 32% martensite and 41% bainite. The higher the volume of martensite, the greater effect that tempering would have on the material's hardness.

5.3 Differences in Mechanical Properties, Global Formability and Local Formability Between the CP 980 and DP 980 Welded Samples

5.3.1 Mechanical Properties of welded CP 980 and DP 980 samples

During uniaxial tension testing, one significant difference observed between the two materials was the location of the failure on the welded samples. The CP steel failed in the base metal in both the longitudinal and transverse directions whereas the DP steel failed in the HAZ.

It has been seen that when DP steel is laser welded and exposed to uniaxial tensile testing, it fails in the soft zone of the HAZ [37] due to the decrease in strength caused be the tempered martensite. This suggests that, since the CP steel failed in the base metal, the soft zone did not have a significant effect on the base metal tensile properties as compared to the DP steel. These observations will be discussed and explained in both in the global formability and local formability analyses.

5.3.2 Global Formability of welded CP 980 and DP 980 samples

Previous research has shown that when laser welded DP samples were subjected to limiting dome height (LDH) test, the sample failed in the soft zone of the weld, which contained tempered martensite, rather than the BM [37], [43], [54], [55]. This trend was also seen during the testing of the DP steel during formability tests but was not seen in the LDH and bi-axial stretch tests performed on the CP steel.

The bi-axial stretch strain analyses on the CP steel, outlined in Figure 4.25, showed that the strain measurements decreased in the areas of the welds. The welds changed the formability by restricting the flow of material and caused the surrounding material to accommodate for the restriction. The bi-axial strain data suggests that the microstructures in the FZ and HAZ are responsible for restricting material flow during forming. On the welded CP steel samples, the crack propagated across the top of the dome, in a direction perpendicular to the welds i.e. the direction of the failure happened regardless of the orientation of the weld with respect to the material's RD. The failures initiated at the weld once the strain level exceeded the capacity of the weld. Since the failure did not travel along the weld, it suggests that the weld's soft zone did not influence propagation direction of the failure. This would also explain why the CP steel failed in the base metal during uniaxial tension testing. The failure traveled along the path which contained the highest amount of strain.

In comparison, the bi-axial stretch strain analyses for the DP steel, outlined in Figure 4.31, showed that the strain measurements increased in the areas of the welds. With the strain concentrating in the HAZ, it was expected that the failure would propagate along this path. These observations can be attributed to the microstructures present within the HAZ. In the DP steel, the size of the soft zone is related to the effects of tempering on the martensite. The soft zone became a stress and strain concentration area and was a significant factor in the decrease in formability as the failure propagated along the soft zone.

5.3.3 Local Formability of welded CP 980 and DP 980 samples

Due to the nature of the hole expansion test apparatus, the conical punch stays in contact with the circumferential material of the sample as it increases the strain. This creates an equal instantaneous-edge-strain around the circumference of hole, eliminating the ability of the material to strain in different areas around the hole. This causes the material within a welded sample to fail in the area that does not respond well to edge strain – regardless if it is in the base metal or in the HAZ.

When hole expansion tests were performed on the welded CP steel, the average λ decreased from 30% (BM) to 21% (welded samples). Previous studies [23], [48] have suggested that edge stretch performance decreases as the hardness difference between the phases within the microstructure increases, which can explain the decrease in λ in these tests. The different microstructures within the CP steel's HAZ, associated with the hardness profile, would have larger hardness differences between the phases as compared to the base metal. These areas contained microstructures that would have the largest difference in hardness between the phases: ferrite and martensite. Therefore, it is not surprising that this was the location of the failure. The hardness, and associated strength of the soft zone would not benefit the edge stretch performance since the strain could not concentrate in these areas like they did during the biaxial stretch test – as explained at the beginning of this section. This data highlights that the presence of laser welds in this CP steel had a significant, negative effect on the local formability of the base metal.

When hole expansion tests were performed on the welded DP steel, the average λ decreased from 11% (BM) to 9% (welded samples). This decrease is not as significant as compared to the CP welded samples. An import point of difference between the DP and CP steel was the location of the edge stretch failure. The welded CP steel samples failed in the HAZ, but the welded DP steel samples failed in the base metal. This can be explained by the fact that the base metal microstructure was ferrite and martensite and that the HAZ microstructure was similar, thus having similar hardness differences between the phases within the different sub-zones within the HAZ. During this test, it is acknowledged that the base metal microstructure was more sensitive to edge strain than the HAZ. This data highlights that the presence of laser welds in this DP material had an insignificant effect on the local formability of the base metal.

Chapter 6

6.0 Conclusions as they Relate to the Research Objectives

Two AHSSs with a minimum tensile strength of 980 MPa were examined during this research. The objective of the research was to understand the fundamental differences between the two steels and how this information can be translated into practical, industry-relevant solutions. The knowledge gained through this research can assist in the proper application of these types of steels, which can mitigate costs for end-user. This research was accomplished by the following:

1. Characterize the two base metals with respect to their chemistry, microstructure, mechanical properties and formability;
2. Determine an optimum fiber-laser welding process for "Bead-On-Plate" welds for each of the steels and;
3. Document the effects the weld had on the mechanical properties, global formability and local formability of the base metals.

6.1 CP 980 Cold Rolled, Un-coated Base Metal Research Conclusions

For the CP 980 AHSS, the following conclusions were drawn from the study:

1. The microstructure of the CP steel was made up of bainite, martensite and ferrite. The bainite was the dominant microstructure, followed by martensite and ferrite.
2. The thermal cycle introduced by the laser during welding created four distinct zones within the HAZ that exhibited unique microstructures which differed from the base metal. These microstructures could be correlated with the hardness-profile of the weld. The SCHAZ showed a decrease in hardness due to the decomposition of martensite to tempered

martensite. However, due to the stability of bainite, tempering had no considerable effect on this phase. The fast cooling rates within the FZ, and UCHAZ created hard zones which were dominated with martensite microstructures. The ICHAZ exhibited a martensite and ferrite microstructure with no presence of bainite.

3. Welded samples exhibited a decrease in elongation (uniaxial tension) and global formability (LDH and bi-axial stretch) as compared to the base metal. This was attributed to the martensitic microstructures developed within the FZ, UCHAZ and ICHAZ. These regions restricted material flow during deformation, forcing the failure to propagate through the base metal and not in the weld HAZ. The bi-axial stretch tests showed that when the welds were positioned equal-to-or-greater-than 19mm from the center line, they had an insignificant effect on the global formability performance of the base metal.
4. The crack produced during bi-axial stretch tests initiated at the HAZ and propagated perpendicular to the weld regardless of its orientation (with respect to the material's rolling direction). This suggests that the crack propagated along the high strain path - across the forming punch - rather than following the weld's soft zone (SCHAZ). This also implies that the soft zone of the weld was not as influential in the failure as compared to the harder zones (FZ, UCHAZ and ICHAZ) of the weld.
5. Welded samples exhibited a decrease in hole expansion (local formability) as compared to the base metal. The failure initiated in the HAZ suggests that microstructure in the HAZ was more sensitive to edge stretch than the base metal. The martensite and ferrite microstructure in the ICHAZ would have created a microstructure with a large strength difference between the phases which is detrimental to edge stretch performance.

6.1 DP 980 HDGA Base Material Research Conclusions

For the DP 980 AHSS, the following conclusions were drawn from the study:

1. The energy per unit area of weld was higher for the HDGA material when compared to the bare CAL material. This was due to the plasma cloud created through the vaporization of the zinc coating during welding. This cloud causes the laser to be absorbed, decreasing the laser power density.
2. The thermal cycle introduced by the laser during welding created 4 distinct zones within the HAZ that exhibited unique microstructures which differed from the base metal. These microstructures could be correlated with the hardness-profile of the weld. The SCHAZ showed a decrease in hardness due to the decomposition of martensite to tempered martensite. The fast cooling rates within the FZ, and UCHAZ created hard zones which were dominated with martensite microstructures. The ICHAZ exhibited a martensite and ferrite microstructure.
3. Welded samples exhibited a decrease in elongation (uniaxial tension) and global formability (LDH and bi-axial stretch) as compared to the base metal. This was attributed to the tempered martensitic microstructure located in the SCHAZ. Strain concentrated in this region, causing failure.
4. The crack produced during bi-axial stretch tests initiated at, and propagated along, the HAZ when the welds which were less-than-or-equal-to 19mm from the forming center line. This implies that the soft zone was an area that the strain localized and that the weld was a significant contributor to the failure of welded samples.
5. During global formability testing, when the welds were positioned greater-than 19mm form the center line, the failure initiated, and propagated, through the base metal. This

suggests that the crack propagated along the high strain path - across the forming punch - rather than following the weld's soft zone (SCHAZ).

6. Welded samples exhibited a slight decrease in hole expansion (local formability) as compared to the base metal. The failure initiated in the base metal and not the HAZ suggesting that the martensite and ferrite microstructure in the base metal was more sensitive to edge stretch than the microstructures present in the HAZ.

References

[1] AISI, “AISI Automotive Market - The Value of Steel in the Automotive Industry.” [Online]. Available: www.steel.org/steel-markets/automotive .

[2] NHTSA, “Research Data - Crashworthiness.” [Online]. Available: https://www.nhtsa.gov/research-data/crashworthiness.

[3] S. Keeler, M. Kimchi, and P. J. Mooney, “WorldAutoSteel Advanced High-Strength Steels Application Guidelines Version 6.0,” 2016.

[4] N. Fonstein, *Advanced High Strength Sheet Steels*. New York: Springer, 2015.

[5] W. D. J. Callister, *Fundamentals of Materials Science and Engineering/An Interactive e-text*, Fith Editi. New York: John Wiley and Sons, Inc., 2001.

[6] M. Y. Demeri, *Advanced High-Strength Steels - Science, Technology and Applications*. Materials Park: ASM International, 2013.

[7] R. G. Davies, “Influence of martensite composition and content on the properties of dual phase steels,” *Metall. Trans. A*, vol. 9, no. 5, pp. 671–679, 1978.

[8] D. R. Askeland and P. P. Phule, *The Science and Engineering of Materials*, Fith Editi. Stamford: Cengage Learning, 2008.

[9] R. A. Higgins, *Engineering Metallurgy - 1. Applied Physical Metallurgy*. London: The English Universities Press Lt., 1973.

[10] P. H. O. M. Alves, M. S. F. Lima, D. Raabe, and H. R. Z. Sandim, “Laser beam welding of dual-phase DP1000 steel,” *J. Mater. Process. Technol.*, vol. 252, no. August 2017, pp. 498–510, 2018.

[11] M. A. Wells and A. Bardelcik, “Course Notes - University of Guelph: ENGG6090 Press Hardening of Steel and Aluminum.” 2019.

[12] H. K. D. H. Bhadeshia, *Bainite in Steels*, Second. London: IOM Communications Ltd., 2001.

[13] G. W. Dallin, “Hot Dipped Galvanizing Training.” Galvinfo Center - International Zinc Association, 2017.

[14] M. Maalekian, “Technische Universität Graz Christian Doppler Laboratory for Early Stages of Precipitation The Effects of Alloying Elements on Steels (I),” no. October, 2007.

[15] K. W. Andrews, “Empirical formulae for the calculation of some transformation temperatures,” *J. Iron Steel Inst.*, vol. 230, pp. 721–727, 1965.

[16] B. Pawłowski, “Critical points of hypoeutectoid steel – prediction of pearlite dissolution finich temperature Ac1f,” *J. Achiev. Mater. Manuf. Eng.*, vol. 49, no. 2, pp. 331–337, 2011.

[17] G. E. Linnert, *Welding Metallurgy - Carbon and Alloy Steels*. Miami: American Welding Society, 1994.

[18] W. Steven and A. G. Haynes, “The Temperature of Formation of Martensite and Bainite in Low-Alloy Steels,” *J. Iron Steel Inst.*, vol. 183, no. 8, pp. 349–359, 1956.

[19] ASTM International, “Standard Test Method for Determining Forming Limit Curves 1 Requirements for E6 Terminology Relating to Methods of Mechanical Testing E8/E8M Test Methods for Tension Testing of Metallic Ma-terials E517 Test Method for Plastic Strain Ratio r for Sheet Meta,” vol. i, pp. 1–16, 2019.

[20] Wi. F. Hosford and R. M. Caddell, *Metal Forming - Mechanics and Metallurgy*. Englewood Cliffs: Prentice-Hall, 1983.

[21] M. H. Cai, H. Ding, Z. Y. Tang, H. Y. Lee, and Y. K. Lee, “Strain hardening behavior of high performance FBDP, TRIP and TWIP steels,” *Steel Res. Int.*, vol. 82, no. 3, pp. 242–248, Mar. 2011.

[22] ISO Technical Committee 164, “DRAFT INTERNATIONAL STANDARD, ISO/FDIS 16630, Metallic materials — Sheet and strip — Hole expanding test,” vol. 2017. 2017.

[23] K. Hasegawa, K. Kawamura, T. Urabe, and Y. Hosoya, “Effects of Microstructure on Stretch-flange-formability of 980 MPa Grade Cold-rolled Ultra High Strength Steel Sheets,” *ISIJ Int.*, vol. 44, no. 3, pp. 603–609, 2008.

[24] N. Pathak, C. Butcher, and M. Worswick, “Assessment of the Critical Parameters Influencing the Edge Stretchability of Advanced High-Strength Steel Sheet,” *J. Mater. Eng. Perform.*, vol. 25, no. 11, pp. 4919–4932, 2016.

[25] H. Kagechi, “Recent Progress and future Trends in the research and development of steels,” *NKK Tech. Rev.*, 2003.

[26] K. Sakata, S. Matsuoka, and K. Sato, “Highly formable sheet steels for automobile through advanced microstructure control technology,” *Kawasaki Steel Tech. Rep.*, no. 48, pp. 3–7, 2003.

[27] T. Shimizu, Y. Funakawa, and S. Kaneko, “High strength steel sheets for automobile suspension and chassis use - High strength hot-rolled steel sheets with excellent press formability and durability for critical safety parts,” *JFE Tech. Rep.*, no. 4, pp. 25–31, Nov. 2004.

[28] N. Zhou, “Course Notes - University of Waterloo:ME735 Special Topics in Welding and Joining - Laser Welding Processes and Metallurgy.” .

[29] C. Dawes, *Laser Welding - A practical guide*. Cambridge: Abington Publishing, 1992.

[30] K. King Saud University, “Welding Calculations.” [Online]. Available: http://fac.ksu.edu.sa/sites/default/files/welding_calculations.pdf.

[31] H. Di, Q. Sun, X. Wang, and J. Li, “Microstructure and properties in dissimilar/similar weld joints between DP780 and DP980 steels processed by fiber laser welding,” *J. Mater. Sci. Technol.*, vol. 33, no. 12, pp. 1561–1571, 2017.

[32] J. E. Lancaster, *Metallurgy of Welding*, Fourth Edi. London: Allen & Unwin Publishers Ltd., 1987.

[33] C. N. Davies and K. Gjermundsen, “Distribution of Temperatures in Arc Welding,” *Br. Weld J.*, vol. 12, pp. 54–74, 1965.

[34] G. Miyamoto *et al.*, “Ref 15 2005 Effect of PAGS on crystallography and morphology of lath martensite,” *Acta Mater.*, vol. 63, no. 9, pp. 202–214, 2018.

[35] T. Hanamura, S. Torizuka, S. Tamura, S. Enokida, and H. Takech, “Effect of austenite grain size on the mechanical properties in air-cooled 0.1c-5Mn martensitic steel,” *Mater. Sci. Forum*, vol. 783–786, no. 12, pp. 1027–1032, 2014.

[36] C. Celada-Casero, J. Sietsma, and M. J. Santofimia, “The role of the austenite grain size in the martensitic transformation in low carbon steels,” *Mater. Des.*, vol. 167, 2019.

[37] N. Sreenivasan, M. Xia, S. Lawson, and Y. Zhou, “Effect of Laser Welding on Formability of DP980 steel,” *J. Eng. Mater. Technol.*, vol. 130, no. 4, p. 041004, 2008.

[38] M. . Xia, E. Biro, Z. L. Tian, and Y. N. Zhou, “Effects of Heat Input on and Martensite on HAZ Softening in Laser Welding of Dual Phase Steels,” *ISIJ Int.*, vol. 48, no. 6, pp. 809–814, 2008.

[39] S. K. Panda, V. H. Baltazar Hernandez, M. L. Kuntz, and Y. Zhou, “Formability analysis of diode-laser-welded tailored blanks of advanced high-strength steel sheets,” *Metall. Mater. Trans. A Phys. Metall. Mater. Sci.*, vol. 40, no. 8, pp. 1955–1967, 2009.

[40] N. Farabi, D. L. Chen, J. Li, Y. Zhou, and S. J. Dong, “Microstructure and mechanical properties of laser welded DP600 steel joints,” *Mater. Sci. Eng. A*, vol. 527, no. 4–5, pp. 1215–1222, 2010.

[41] X. N. Wang, Q. Sun, Z. Zheng, and H. S. Di, “Microstructure and fracture behavior of laser welded joints of DP steels with different heat inputs,” *Materials Science and Engineering A*, vol. 699. pp. 18–25, 2017.

[42] N. Farabi, D. L. Chen, and Y. Zhou, “Microstructure and mechanical properties of laser welded dissimilar DP600/DP980 dual-phase steel joints,” *J. Alloys Compd.*, vol. 509, no. 3, pp. 982–989, 2011.

[43] M. S. Xia, M. L. Kuntz, Z. L. Tian, and Y. Zhou, “Failure Study on Laser Welds of Dual Phase Steel in Formability Testing,” *Sci. Technol. Weld. Join.*, vol. 13, no. 4, pp. 378–387, 2008.

[44] D. Westerbaan *et al.*, “Effects of concavity on tensile and fatigue properties in fibre laser welding of automotive steels,” *Sci. Technol. Weld. Join.*, vol. 19, no. 1, pp. 60–68, 2013.

[45] W. Xu *et al.*, “Microstructure and fatigue performance of single and multiple linear fiber laser welded DP980 dual-phase steel,” *Mater. Sci. Eng. A*, vol. 553, pp. 51–58, 2012.

[46] Japanese Standards Association, “JIS Z 2241 - Method of tensile test for metallic materials.” Japanese Standards Association, 1993.

[47] ASTM International, "ASTM Standard E562-02 Standard Test Method for Determining Volume Fraction by Systematic Manual Point Count," *ASTM Book of Standards*, no. C. pp. 1–7, 2002.

[48] V. Flaxa and S. Kluge, "Microalloyed Low-Carbon Multiphase Steels," *Steel Res. Int.*, vol. 87, no. 10, pp. 1264–1273, 2016.

[49] V. H. Baltazar Hernandez, S. S. Nayak, and Y. Zhou, "Tempering of martensite in dual-phase steels and its effects on softening behavior," *Metall. Mater. Trans. A Phys. Metall. Mater. Sci.*, vol. 42, no. 10, pp. 3115–3129, 2011.

[50] H. K. D. H. Bhadeshia and R. W. K. Honeycombe, *Steels*, Fourth. Cambridge: Butterworth-Heinemann, 2017.

[51] H. K. D. H. Bhadeshia, *Bainite in steels, second edition*, vol. 21A. IOM Communications Ltd, 2001.

[52] M. Y. Tu, C. A. Hsu, W. H. Wang, and Y. F. Hsu, "Comparison of microstructure and mechanical behavior of lower bainite and tempered martensite in JIS SK5 steel," *Mater. Chem. Phys.*, vol. 107, no. 2–3, pp. 418–425, 2008.

[53] D. C. Saha, S. S. Nayak, E. Biro, A. P. Gerlich, and Y. Zhou, "Mechanism of Secondary Hardening in Rapid Tempering of Dual-Phase Steel," *Metall. Mater. Trans. A Phys. Metall. Mater. Sci.*, vol. 45, no. 13, pp. 6153–6162, 2014.

[54] M. Xia, N. Sreenivasan, S. Lawson, Y. Zhou, and Z. Tian, "A Comparative Study of Formability of Diode Laser Welds in DP980 and HSLA Steels," *J. Eng. Mater. Technol.*, vol. 129, no. 3, p. 446, 2007.

[55] K. Bandyopadhyay, S. K. Panda, P. Saha, V. H. Baltazar-Hernandez, and Y. N. Zhou, "Microstructures and failure analyses of DP980 laser welded blanks in formability context," *Mater. Sci. Eng. A*, vol. 652, pp. 250–263, 2016.